catalysts

MDPI

Article

Single-Step Synthesized Functionalized Copper Carboxylate Framework Meshes as Hierarchical Catalysts for Enhanced Reduction of Nitrogen-Containing Phenolic Contaminants

Po-Hsin Mao [1], Nguyen Nhat Huy [2,3], Suresh Ghotekar [4], Jia-Yin Lin [1], Eilhann Kwon [5], Fei-Yee Yeoh [6], Farshid Ghanbari [7,*], Grzegorz Lisak [8,9] and Kun-Yi Andrew Lin [1,*]

1 Department of Environmental Engineering & Innovation and Development Center of Sustainable Agriculture, National Chung Hsing University, 250 Kuo-Kuang Road, Taichung 402, Taiwan; mao29710@gmail.com (P.-H.M.); jerrica1119@gmail.com (J.-Y.L.)
2 Faculty of Environment and Natural Resources, Ho Chi Minh City University of Technology (HCMUT), Ho Chi Minh City 700000, Vietnam; nnhuy@hcmut.edu.vn
3 Vietnam National University Ho Chi Minh City, Ho Chi Minh City 700000, Vietnam
4 Department of Chemistry, Smt. Devkiba Mohansinhji Chauhan College of Commerce & Science, University of Mumbai, Silvassa 396 230, Dadra and Nagar Haveli (UT), India; ghotekarsuresh7@gmail.com
5 Department of Earth Resources and Environmental Engineering, Hanyang University, SeongDong-Gu, Seoul 133-791, Korea; ek2148@hanyang.ac.kr
6 School of Materials and Mineral Resources Engineering, Engineering Campus, Universiti Sains Malaysia, Nibong Tebal, Pulau Pinang 14300, Malaysia; yeoh.usm@gmail.com
7 Department of Environmental Health Engineering, Abadan Faculty of Medical Sciences, Abadan 6313833177, Iran
8 School of Civil and Environmental Engineering, Nanyang Technological University, 50 Nanyang Avenue, Singapore 639798, Singapore; g.lisak@ntu.edu.sg
9 Residues and Resource Reclamation Centre (R3C), Nanyang Environment and Water Research Institute, Nanyang Technological University, 1 Cleantech Loop, Clean Tech One, Singapore 637141, Singapore
* Correspondence: ghanbari.env@gmail.com (F.G.); linky@nchu.edu.tw (K.-Y.A.L.)

check for updates

Citation: Mao, P.-H.; Huy, N.N.; Ghotekar, S.; Lin, J.-Y.; Kwon, E.; Yeoh, F.-Y.; Ghanbari, F.; Lisak, G.; Lin, K.-Y.A. Single-Step Synthesized Functionalized Copper Carboxylate Framework Meshes as Hierarchical Catalysts for Enhanced Reduction of Nitrogen-Containing Phenolic Contaminants. *Catalysts* **2022**, *12*, 765. https://doi.org/10.3390/catal12070765

Academic Editor: Carolina Belver

Received: 4 May 2022
Accepted: 23 June 2022
Published: 11 July 2022

Publisher's Note: MDPI stays neutral with regard to jurisdictional claims in published maps and institutional affiliations.

Abstract: Nitrogen-containing phenolic contaminants (NCPCs) represent typical pollutants of industrial wastewaters. As catalytic reduction of NCPCs is a useful technique and Cu is an efficient metal catalyst, Cu-carboxylate frameworks (CuCF) are favorable materials. However, they are in powder form, making them difficult to use; thus, in this study, CuCF was grown on macroscale supports. Herein, we present a facile approach to develop such a CuCF composite by directly using a Cu mesh to grow CuCF on the mesh through a single-step electrochemical synthesis method, forming CuCF mesh (CFM). CFM could be further modified to afford CuCF mesh with amines (NH_2) (CFNM), and CuCF mesh with carboxylates (COOH) (CFCM). These CuCF meshes are compared to investigate how their physical and chemical characteristics influenced their catalytic behaviors for reduction/hydrogenation of NPCPs, including nitrophenols (NPs) and dyes. Their nanostructures and surface properties influence their behaviors in catalytic reactions. In particular, CFCM appears to be the most efficient mesh for catalyzing 4-NP, with a much higher rate constant. CFCM also shows a significantly lower E_a (28.1 kJ/mol). CFCM is employed for many consecutive cycles, as well as convenient filtration-type 4-NP reduction. These CuCF meshes can also be employed for decolorization of methylene blue and methyl orange dyes via catalytic hydrogenation.

Keywords: copper; MOFs; mesh; catalytic reduction; dyes; nitrophenol

1. Introduction

Nitrogen-containing phenolic contaminants (NCPCs) are almost ubiquitous in industrial wastewaters [1]. Amidst numerous NCPCs, nitrophenols (NPs) have been increasingly concerning, since NPs can interfere with the nerve/blood systems of the human body [2]. Thus, several methods (e.g., physical, chemical, and biological techniques [3,4]) have been

developed for removing NPs, especially 4-NP, from wastewaters to prevent its harmful impact. Among these various techniques, chemically reductive treatment of 4-NP represents an advantageous technique, as the toxic nitro group of 4-NP can then be catalytically transformed to a less-toxic amine moiety, affording 4-aminophenol (4-AP); this is especially advantageous because 4-AP is a valuable molecule that can be used for the synthesis of chemical products [5–10].

For reducing 4-NP to 4-AP, reducing agents (i.e., $NaBH_4$), together with noble metals (including Ru, Au, etc.), are frequently required [11,12]. Nonetheless, high costs of noble metal catalysts impede realistic implementation of this technology. Hence, it would be more practical to create alternative materials (without usage of noble metals) for the reduction of NPs. In recent times, a special family of porous coordination polymers, called "metal–organic frameworks (MOFs)" has been developed [13–15]. MOFs can be synthesized using various non-noble metals and different ligands to create well-defined porous structures with versatile physical/chemical properties [13], making MOFs advantageous catalysts for a variety of reactions [16–18].

Among these non-noble metals, Cu, Co, Ni, etc., have been also evaluated [3,19–21], and Cu is considered as one of the most effective non-noble metal catalysts because Cu and Cu-oxides can effectively mediate electron-transfer processes between the reducing agent and 4-NP for hydrogeneration of 4-NP to 4-AP [3,19,22]. Cu-based MOFs, especially those containing Cu–O clusters, would be favorable candidates for 4-NP reduction. To this end, carboxylate ligands are particularly attractive and useful as carboxyl groups of ligands can coordinate with Cu to afford the Cu–O clusters within MOFs. Therefore, a relatively inexpensive and highly accessible carboxylate ligand, benzene-1,4-dicarboxylic acid (BDC), is here chosen to coordinate with Cu to form Cu-carboxylate frameworks (CuCF).

While CuCF might be a useful non-noble metal catalyst in reducing 4-NP, CuCF typically exists as nanoparticles, which would be impractical for pragmatic applications. Therefore, it is critical to decorate CuCF on supports, especially macroscale supports, in order to make such a CuCF composite convenient for use. The resultant composite of nanostructured CuCF with macroscale supports can be referred to as a "hierarchical" structure which would represent combinations of different scales of materials for increasing accessibility of active sites in nanostructures and facilitating convenient operation by macroscale supports [6,22–24].

More importantly, this type of CuCF composite should be prepared simply without complex protocols, and the reagents to make these CuCF composites should be more promising and practical. Herein, we propose a facile approach to develop such a CuCF composite by directly using a macroscale Cu mesh to grow nanoscale CuCF on the mesh through a single-step electrochemical synthesis method. The Cu mesh was particularly selected because Cu mesh can be directly used as a source of Cu, and the mesh configuration provides a large surface for growing CuCF to form hierarchical structures, allowing it to be exposed to reactants easily. For instance, Wang et al. claimed to establish a hierarchical material by employing a copper mesh with a macroscale configuration, on which nanoclusters of Cu_2O were deposited via an electrochemical method to form a "hierarchical composite" [22]. On the other hand, Guo et al. claimed to build up a hierarchical material by using a stainless steel mesh as a macroscale support, on which nanostructured ZnO nanorod-array was then deposited [23]. Furthermore, Xiong et al. also claimed to develop a hierarchical material by growing a Zr-based MOFs polyacrylonitrile mesh for enhancing activities [24].

Moreover, the mesh configuration can also act a filter, allowing reactants to flow directly through the mesh for further catalytic reactions. On the other hand, since catalytic reductive reactions of NCPCs would certainly involve surficial interactions between catalysts and reactants, surface properties are of importance to govern behaviors of catalysts. Thus, in this study, CuCF meshes are further modified to possess different functional groups, especially amine and carboxylate groups, by using functionalized carboxylate ligands during the electrochemical fabrication of CuCF meshes. Specifically, CuCF mesh

without additional functional group would be denoted as CFM, whereas CuCF meshes with amines and carboxylates would be denoted as CFNM, and CFCM, respectively.

CuCFs with different functional groups have been also reported for aqueous applications [25–27]. For instance, CuCF has been applied as an adsorbent for the removal of methylene blue from water, and CuCF exhibited superior stability in an aqueous environment and maintained stable and durable adsorption capacities [25]. CuCF with an amine functional group has been also employed as an adsorbent, and a catalyst for removing dyes in aqueous environments, and retained a superior stability for multiple-cycle applications [26]. In addition, CuCF with a carboxylate group has also been applied as an adsorbent for removing malachite green from water, and maintained high stability and durability for consecutive operation without significant destruction in its structure [27].

Through investigating these CuCF meshes for the reduction of NPs, as well as other NCPCs, the relationship between different physical/chemical/surficial properties and catalytic behaviors of CuCF meshes can be then revealed to provide insights for designing and optimizing CuCF meshes for catalytic reductive applications.

2. Results

2.1. Characterization of CuCF Meshes

Fabrication of CuCF meshes is illustrated in Figure 1a. Since CuCF meshes were fabricated using pristine Cu meshes, the appearance of Cu mesh can be visualized in Figure 1b, exhibiting the typical reddish brown color and a very dense woven structure. Its microscale morphology is revealed in Figure S1, in which Cu rounded wires with a diameter of ~50 μm were woven perpendicularly to afford the mesh with a hole size of ~80 μm. The pristine Cu mesh also exhibited very smooth surfaces, as shown in Figure S1b, and no specific substances/patterns were present.

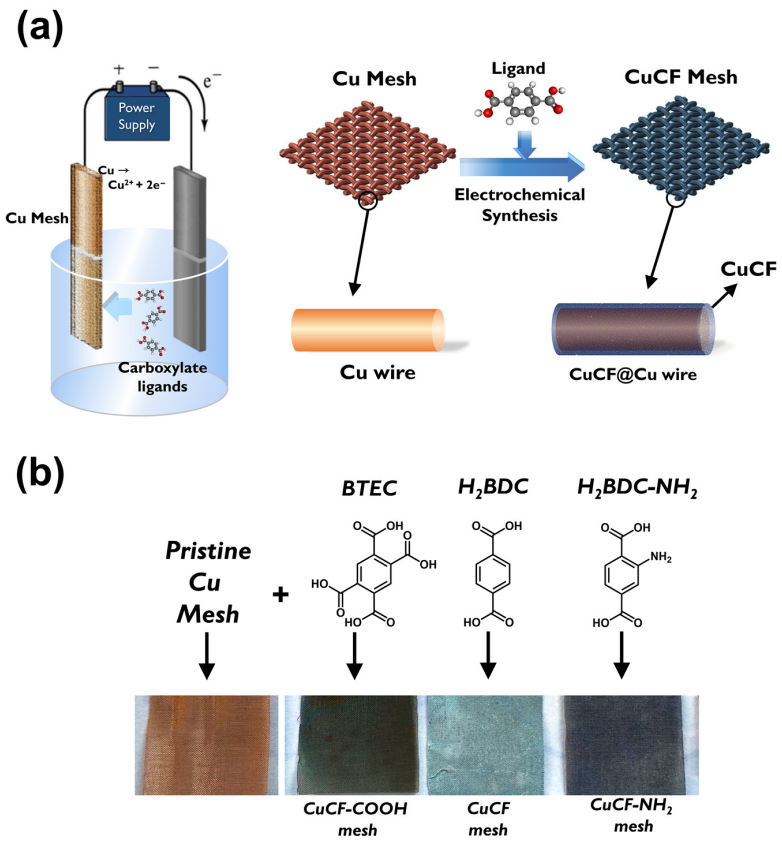

Figure 1. (**a**) Scheme of preparation of CuCF meshes via one-step electrochemical syntheses; (**b**) pictures of resultant CuCF meshes.

Once the pristine Cu mesh was modified by electrochemical anodization in the presence of carboxylate ligands, the reddish brown color of Cu mesh was noticeably changed to a color of dark gray, as shown in Figure 1b, suggesting that the Cu meshes had been modified and deposited with certain substances. Figure 2 further reveals microscopic morphologies of these modified Cu meshes. Specifically, Figure 2a shows the electrochemically synthesized Cu mesh in the presence of BDC, and presents how the Cu wires were fully covered by innumerable fluffy needles. Figure 2b unveils that the needles exhibited a thickness of ~200 nm and a length of a few micrometers. These images also demonstrate that the single-step electrochemical anodization of Cu mesh in the presence of BDC successfully grew nanostructures on Cu meshes. Elemental analysis of the BDC-modified Cu mesh presents how signals of C, O and Cu (Figure 3a) were uniformly distributed all over the Cu mesh, indicating that these resulting nanostructures were evenly grown on the Cu mesh. The abundant signals of C and O elements also validate that the BDC ligand shall be incorporated and comprised in these nanostructures.

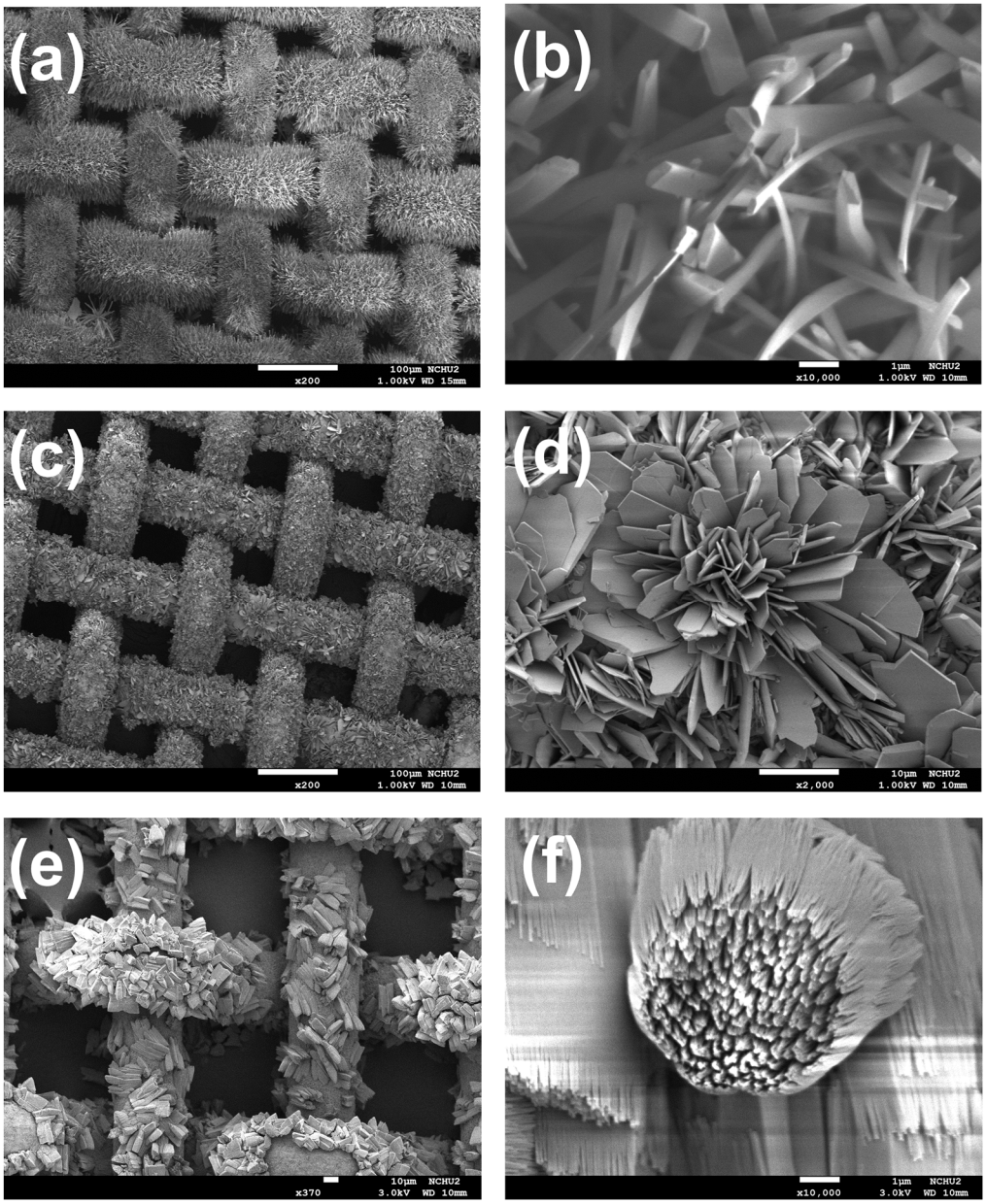

Figure 2. SEM images of (**a**,**b**) CFM, (**c**,**d**) CFNM and (**e**,**f**) CFCM under different magnifications.

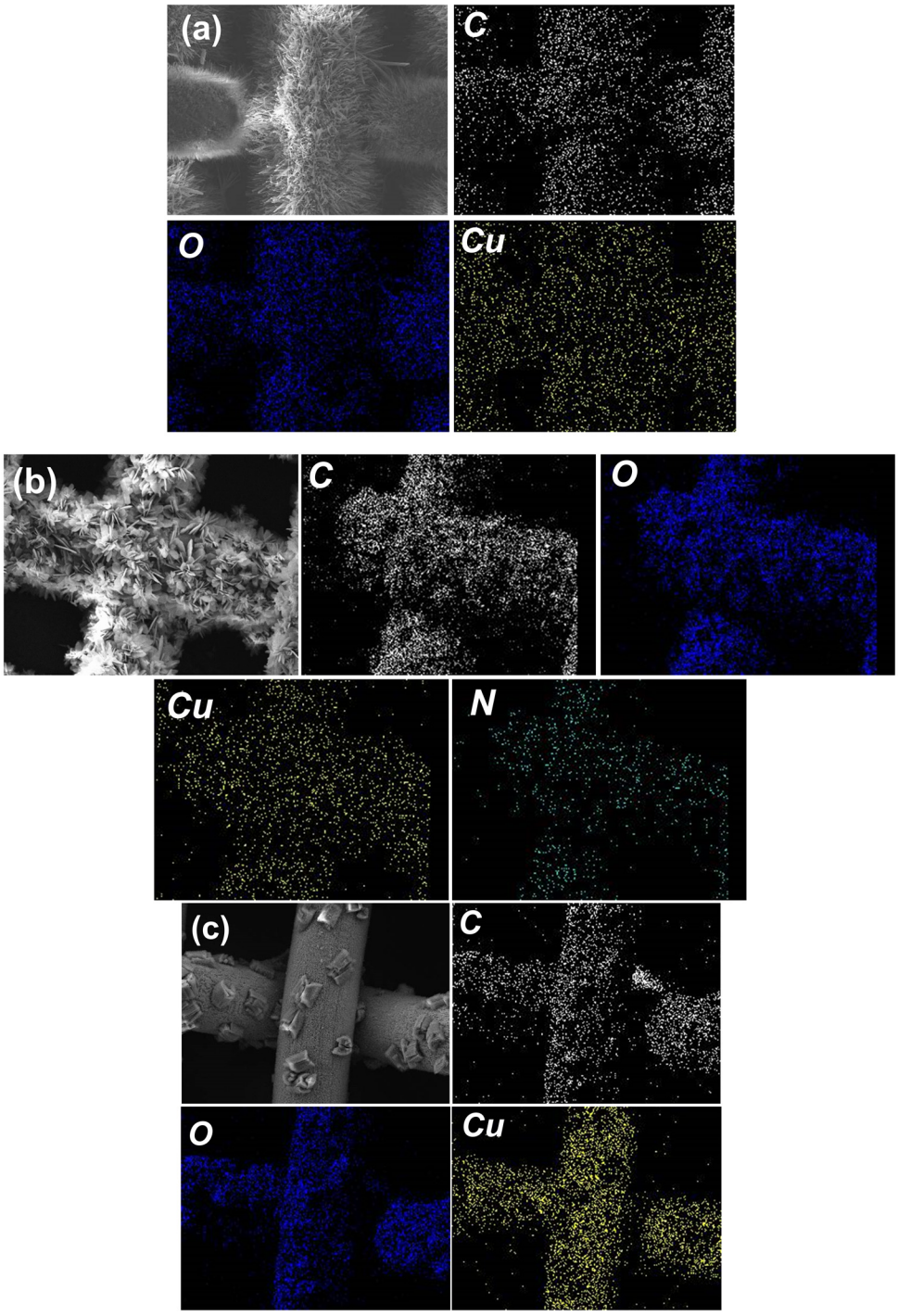

Figure 3. Elemental mapping images of (**a**) CFM, (**b**) CFNM and (**c**) CFCM.

When BDC-NH_2 was then used as another carboxylate ligand in the electrochemical anodization of Cu mesh (the resultant modified Cu mesh can be observed in Figure 1b), the original reddish brown Cu mesh was also transformed to the gray-colored mesh. Its corresponding SEM (Figure 2c) also reveals that the Cu wires were also fully covered by sheet-like substances. Figure 2d further unveils the microscale morphologies of these sheet-like substances, which were actually comprised of very thin nanosheets assembled to afford nanoflower-like nanostructures. Figure 3b further reveals the corresponding elemental mapping result, and signals of C, O, Cu and even N were also uniformly spread

over the entire mesh, indicating that BDC-NH_2 had been successfully incorporated into these nanoflower-like nanostructures.

As BTEC was then employed, the color of the pristine Cu mesh noticeably varied to gray (Figure 1b), indicating that certain substances had grown on the Cu mesh. Its corresponding SEM image (Figure 2e) unveils that these Cu wires were decorated and covered by clusters of chunks, which were actually comprised of bundles of nanofibers. On the other hand, Figure 3c also reveals signals of C, O and Cu evenly distributed over the mesh, and BTEC was also incorporated into these nanostructures comprised of bundles of nanofibers.

These characterizations validate that the single-step electrochemical anodization of Cu mesh in the presence of carboxylate ligands would successfully grow nanostructures comprised of Cu, and ligands. To further investigate these nanostructures, the crystalline structures are shown in Figure 4a. Prior to growing these nanostructures, the pristine Cu mesh exhibited three noticeable signature peaks of Cu metal at 43.3, 50.5 and 74.3° (JCPDS card# 65-9473) [28]. After electrochemical anodization with BDC, the XRD analyses of the resultant mesh retained those original signals of Cu mesh; nevertheless, several additional peaks could be found at 8~40°, and the corresponding pattern can be indexed properly according to the simulated pattern CuBDC MOF [29], suggesting that the fluffy needle-like nanostructures could be ascribed to CuBDC MOF, and the resultant modified mesh was a CuMOF mesh.

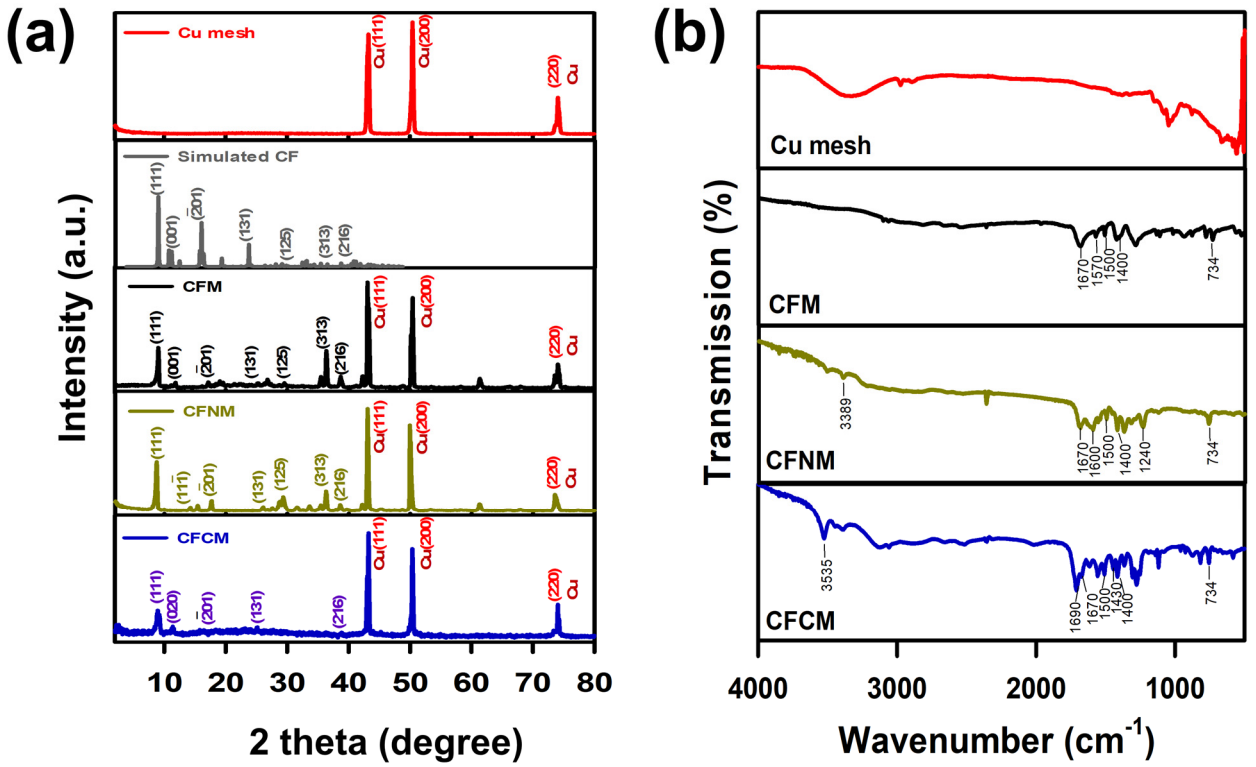

Figure 4. (**a**) XRD patterns, and (**b**) IR spectra of pristine Cu mesh, CFM, CFNM and CFCM.

The crystalline structure of the modified Cu mesh in the presence of BDC-NH_2 was also obtained; the peaks of Cu metal were preserved, and a number of peaks in 8~40° were also observed, which could be indexed properly based on the reported pattern of CuBDC MOF [29], suggesting that CuBDC-NH_2 MOF had been successfully grown on the Cu mesh. The Cu mesh after the electrochemical anodization in the presence of BTEC is revealed in Figure 4a, in which the typical peaks of Cu metals could be observed, and a few additional peaks were also observed. The coordination of Cu–BTEC has been reported to exhibit a comparable structure based on the prototype configuration of CuBDC [27,29]. Therefore,

similar to the aforementioned CuMOF meshes, the resultant Cu mesh with BTEC also exhibited several peaks in the range of 8~40°, which were also indexed properly to CuBDC as the formation of CuBTEC [30].

On the other hand, IR spectra of these modified Cu meshes were collected, and are displayed in Figure 4b. In comparison to the pristine Cu mesh, these modified Cu meshes showed a number of bands at 700~1850 cm^{-1}, which were characteristic peaks of the carboxylate ligands, as displayed in Figure S2 [31–33]. In particular, the bands at 734 and 1500 cm^{-1} can be ascribed to aromatic rings [31], whereas the bands at 1400 cm^{-1}, as well as 1670 cm^{-1}, correspond to the coordinated carboxylic, and carbonyl groups in BDC-based MOF. Therefore, these IR spectra of modified Cu meshes also demonstrated that the carboxylate ligands were coordinated with Cu in these nanostructures grown on Cu meshes, forming CuCF meshes.

Moreover, when BDC-NH_2 was employed, its spectrum exhibited several additional bands at 1240 and 1600 cm^{-1}, corresponding to the C–N group and N–H group of primary amine [29], and the band at 3388 cm^{-1} could be assigned to the N-H stretching mode derived from BDC-NH_2 [34], as displayed in Figure S2. Therefore, the resultant CuCF was validated to possess the amine functional group; thus, this specific CuCF was then denoted as CuCF–NH_2 mesh (CFNM).

On the other hand, as BTEC was employed as the ligand, its corresponding spectrum also exhibited two noticeable additional bands at 1430 and 1690 cm^{-1}. The peak at 1430 cm^{-1} was attributed to the unbound (free) carboxylate group, whereas the peak at 1690 cm^{-1} was attributed to the non-coordinated carbonyl moiety [30,33]. In addition, the intensity of the band at 3535 cm^{-1}, attributed to the O-H stretching mode [35], was still pronounced. This further indicates that freely unbound carboxylate groups existed in the resultant CuCF fabricated by BTEC. Previous studies have also reported that carboxylate groups would exist in the non-coordinated form in the coordination of Cu and BTEC to possess the functional group of carboxylic acid [32,33]. Thus, this CuCF mesh was then denoted as CuCF–COOH mesh (CFCM).

The surface chemistry of these CuMOF meshes was then investigated by XPS, as shown in Figure 5. For comparison, the full survey of the pristine Cu mesh is also displayed in Figure S3a, in which a noticeable signal of Cu was observed with negligible fractions of C and O, possibly due to impurities and moisture on its surface. Figure S3b reveals the corresponding Cu2p core-level spectrum, in which two tall peaks can be detected at 932.2 and 952.3 eV, ascribed to Cu^0 [36], validating the metal state of Cu mesh.

In addition, once the pristine Cu mesh was fabricated to become CuCF meshes, the corresponding full survey spectra of CuCF meshes were noticeably distinct. In particular, Figure 5a reveals the full survey scan of CFM, in which a dominant signal of Cu was still observed but the fractions of C and O had become considerably higher. This suggests that the surface chemistry of CFM mesh was distinct from that of pristine Cu mesh, as CFM had been grown on the mesh, thereby exhibiting much stronger signals of C and O from the BDC ligand. Moreover, the corresponding Cu2p spectrum unveils a few tall bands at 933.5 and 953.4 eV, both corresponding to Cu^{2+} [3], which can be attributed to the Cu species coordinated in CuBDC MOF [29]. Moreover, a number of bands were noted at 939.4, 943.3, 959.2 and 962.7 eV, which were attributed to the Cu^{2+} satellite peaks [37,38].

In addition, the O1s core-level spectrum of CFM was also analyzed, as shown in Figure 5c, in which three underlying peaks were afforded at 531.2, 532.1 and 532.8 eV, ascribed to Cu–O, O–C=O and absorbed O, respectively. The presence of Cu–O and O–C=O validated the coordination between Cu and carboxylate ligands in CuCF mesh [39].

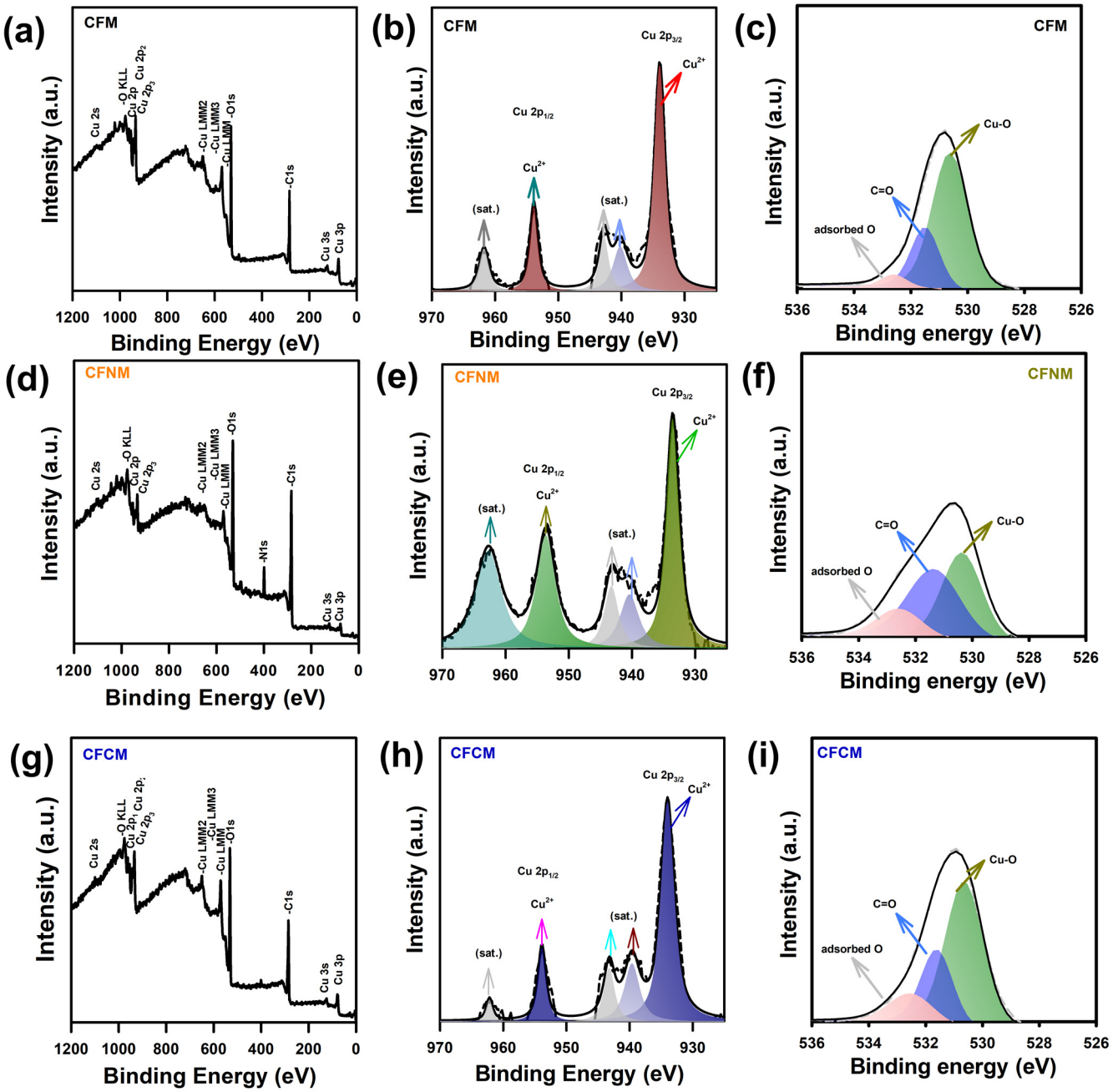

Figure 5. Full survey and core-level XPS analyses of (**a**–**c**) CFM, (**d**–**f**) CFNM and (**g**–**i**) CFCM.

In the case of CFNM, its full survey spectrum (Figure 5d) also exhibited significant signals of Cu, C and O, ascribed to CuCF. Additionally, a noticeable fraction of N was observed at 400 eV, validating the presence of an amine functional group. Figure 5e further unveils the Cu2p core-level spectrum, in which two tall bands at 933.5 and 953.4 eV, attributed to Cu^{2+} [3], and four peaks at 939.4, 943.3, 959.2 and 962.7 eV, corresponding to the Cu^{2+} satellite peaks [37,38], can also be observed. Moreover, the O1s spectrum of CFNM can also be analyzed, as shown in Figure 5f, in which Cu–O, O–C=O and absorbed O can be detected at 531.3, 532.0 and 532.9 eV, respectively [39]. In the case of CFCM, its corresponding full survey spectrum (Figure 5g) also consisted of high fractions of Cu, C and O, ascribed to CuBTEC coordination. Moreover, its Cu2p spectrum, displayed in Figure 5h, reveals how Cu^{2+} species can be also detected at 933.5 and 953.4 eV, whereas its O1s spectrum can be

deconvoluted to afford three peaks at 531.3, 532.0 and 532.9 eV, corresponding to Cu–O, O–C=O and absorbed O, respectively, validating the presence of BTEC.

Moreover, as CuCF meshes were composites comprised of nanoscale CuCF and macroscale meshes, their textural properties could be then analyzed. Figure 6a exhibits N_2 sorption isotherms of pristine Cu mesh, as well as various CuCF meshes. The pristine Cu mesh (without CuCFs) exhibited a sorption isotherm relatively similar to the IUPAC type II isotherm, as the Cu mesh was a macroscale but nonporous support. Its N_2 sorption was relatively low, possibly due to its smooth surface, leading a low surface area of 15 m^2/g. Once the Cu mesh was modified and covered with CuCFs, the corresponding N_2 sorption significantly increased, and the corresponding isotherms were closer to the IUPAC type IV isotherm with noticeable hysteresis loops, suggesting that these CuCF meshes might contain pores (e.g., mesopores). Once Cu mesh was fabricated into CFM, its hysteresis loop could be noticed, possibly owing to the presence of pores from CuCF. Therefore, CFM exhibited a relatively high surface area of 30 m^2/g. Moreover, CFNM, and CFCM also exhibited slightly higher N_2 sorption than the pristine Cu mesh itself. Surface areas of CFNM and CFCM were measured as 25 and 23 m^2/g, respectively. The relatively high surface area of CFM might be attributed to its fluffy needle-like nanostructure, whereas nanofibers were closely packed and formed bundles in CFCM, leading to the relatively low surface area. Then, the pore size distribution and pore volumes of these CuCF meshes were determined. As displayed in Figure S4 (in the supporting information), CFM, CFNM and CFCM all exhibited pores in the range of 2~50 nm, validating that these CuCF meshes contained mesopores. In particular, a relatively large hysteresis loop could be found in CFM possibly because CFM exhibited relatively high pore volumes from the pores in the mesoporous range. The pore volumes of these CuCF meshes were also calculated as CFM, CFNM and CFCM mesh, exhibiting pore volumes of 0.042, 0.036 and 0.018 cm^3/g, respectively.

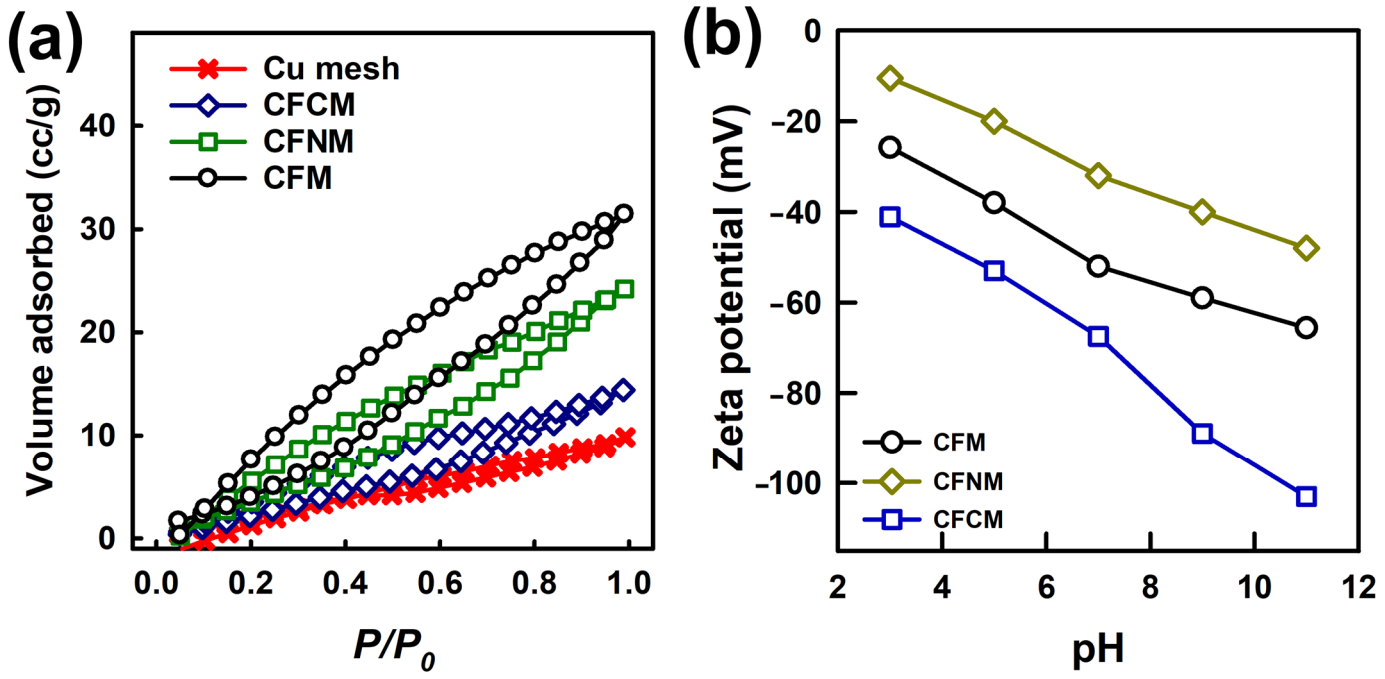

Figure 6. (**a**) N_2 sorption isotherms and (**b**) zeta potentials of CuMOF meshes.

However, the growth of CuCF, affording those nanostructures, on Cu mesh would certainly improve their textural properties, and increase surface contact areas.

Since the reduction of nitrogen-containing contaminants is an aqueous reaction, and CuCF was functionalized with different functional groups, it would be useful to further explore the surface charges of these CuCF meshes [40]. Figure 6b displays the zeta potentials of CuCF meshes, which all exhibited relatively negative charges in the range of pH = 3~11.

In particular, CFM exhibited −25.8 mV at pH = 3, then continuously decreased at increasing pH values, and eventually reached −65.9 mV at pH = 11. On the other hand, CFNM showed −10.5 mV at pH of 3, then also progressively dropped at higher pH values, and then reached −48.0 mV at pH = 11. Moreover, CFCM revealed a surface charge of −41.1 mV at pH = 3, which then continuously decreased, and dropped to −103.0 mV at pH = 11. These results suggest that the functional group of CuCF meshes certainly influenced their surface charges; the amine group might enable CuCF mesh to exhibit less negative charges, whereas the existence of carboxylate groups would enable CFCM to exhibit much more negative surface charges. These surficial properties might then affect their behaviors during catalytic reactions of contaminant reduction. On the other hand, these CuCF meshes were also further analyzed using thermogravimetric (TG) analysis; the corresponding TG curves are displayed in Figure S5. Since the mesh itself was Cu, which would be oxidized in air to become Cu oxides, TG analyses of these CuCF meshes were conducted in N_2. Overall, these CuCF meshes remained relatively stable up to 150 °C, with very slight weight losses possibly due to moisture. Subsequently, these CuCF meshes started to decompose, and underwent a series of weight losses in the range of 300~400 °C because of thermal decomposition of ligands. These TG results demonstrated that these CuCF meshes would be very stable at ambient conditions, especially in the range for aqueous reduction reactions.

2.2. 4-NP Reduction by CuCF Meshes

Before studying these CuCF meshes for reducing 4-NP, it is essential to investigate if 4-NP could be eliminated by these CuCF meshes merely through adsorption towards these CuCF meshes. Figure S6b firstly displays the spectral variation of 4-NP with a pristine Cu mesh (without addition of $NaBH_4$), and the spectrum with a dominant peak at 317 nm remained almost unchanged (C_t/C_0 at 30 min = 1), and no peak of 4-AP, which is located at 300 nm, could be observed, indicating that the pristine Cu mesh cannot remove 4-NP via adsorption or reduction. Figure S6c also reveals that the UV-Vis spectrum of 4-NP in the presence of CFM without addition of $NaBH_4$ was barely changed over 30 min (C_t/C_0 at 30 min = 0.990), suggesting that 4-NP could not be noticeably removed by CFM itself via adsorption, and 4-NP was not reduced to 4-AP. On the other hand, when CFNM was then employed, its corresponding UV-Vis spectrum in the absence of $NaBH_4$ was slightly changed over 30 min (C_t/C_0 at 30 min = 0.959); however, no noticeable peak at 300 nm could be observed as no 4-AP was then produced. This demonstrates that CFNM itself might exhibit a slight affinity towards 4-NP (Figure S6d). In the case of CFCM, a similar result was observed as the UV-Vis spectrum of 4-NP was also slightly changed over 30 min (C_t/C_0 at 30 min = 0.940) (Figure S6d), and no 4-AP was then produced, suggesting that a very small part of 4-NP might be eliminated via adsorption by CFCM rather than reduction.

After $NaBH_4$ was introduced, the absorption peak of 4-NP at 317 nm would be shifted to 400 nm as a result of deprotonation of 4-NP [3,41–43], as shown in Figure 5a. Figure S7 shows UV-Vis spectral variation of 4-NP in the presence of pristine Cu mesh and $NaBH_4$, and the peak of 4-NP at 400 nm was almost unchanged over 150 s, demonstrating that the pristine Cu mesh cannot incorporate with $NaBH_4$ for reducing 4-NP. Figure 7a also shows UV-Vis spectral variation of 4-NP in the presence of CFM, and the peak of 4-NP at 400 nm certainly changed and became noticeably smaller. On the other hand, a short peak at 300 nm was observed, indicating that 4-NP had been converted to 4-AP. Nevertheless, the reduction of 4-NP by CFM could not be completely achieved in 70 s. On the other hand, when CFNM was then employed (Figure 7b), the maximum peak of 4-NP at 400 nm decreased quickly, and almost disappeared in 70 s, whereas the peak of 4-AP raised up noticeably, indicating that transforming 4-NP to 4-AP was achieved in a very short period. On the other hand, when CFCM was used, the peak of 4-NP decreased even faster (Figure 7c), and completely disappeared in 70 s, with the noticeable peak of 4-AP raised up.

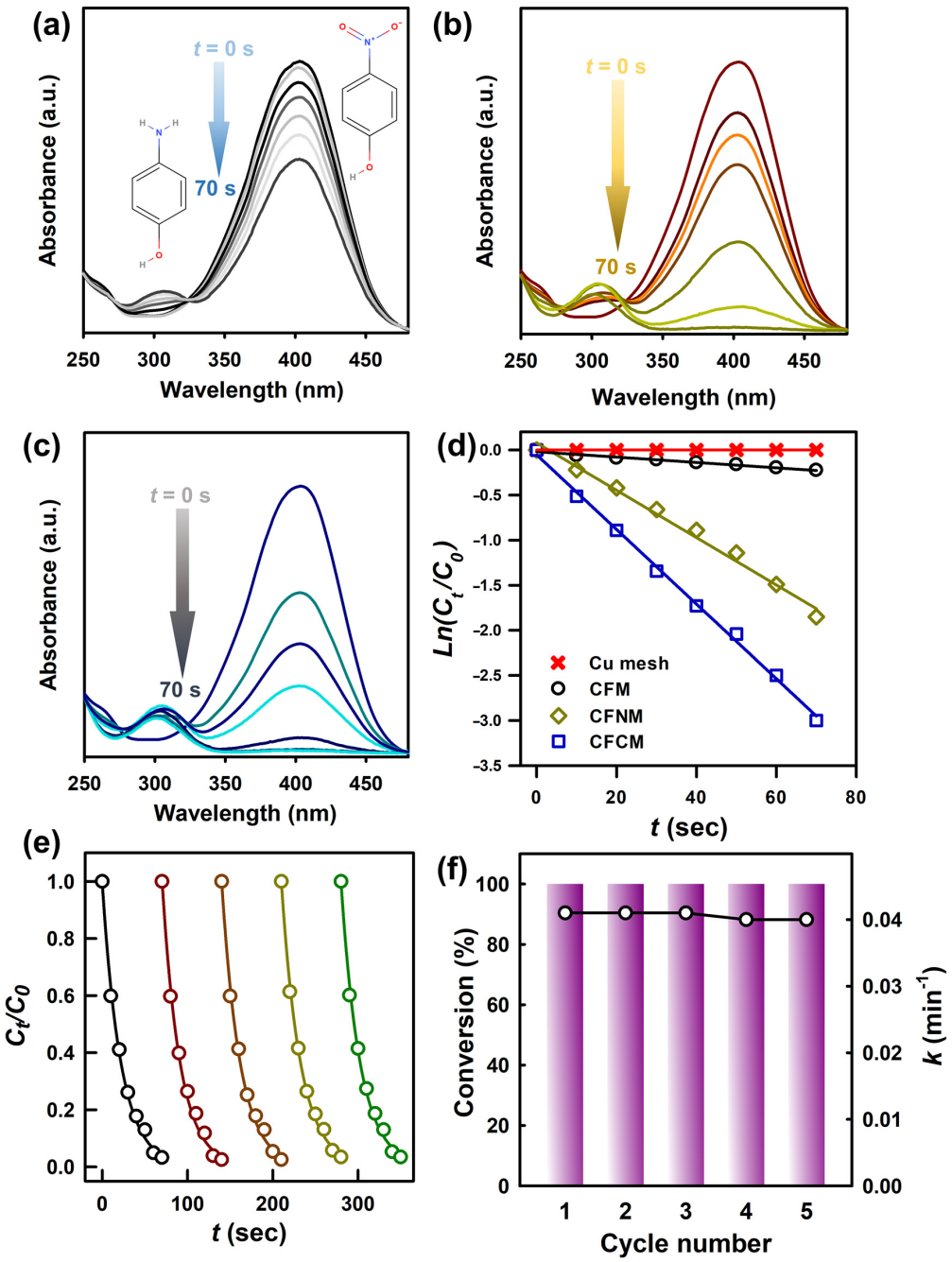

Figure 7. Absorption spectra of 4-NP and 4-AP during reduction by different CuCF meshes: (**a**) CFM, (**b**) CFNM, (**c**) CFCM and (**d**) pseudo-first order plots of 4-NP reduction in the presence of $NaBH_4$ over different meshes at 28 °C. (**e**) Plot of C_t/C_0 against the reaction time for seven successive cycle reactions catalyzed by CFCM; (**f**) conversion and relative change in k for each cycle with CFCM as a catalyst.

For further quantitative comparison of 4-NP reduction by these CuCF meshes, the kinetics of 4-NP reduction was further calculated by variation of 4-NP concentration based on a maximum peak of 4-NP at 400 nm by the following pseudofirst order rate law [22]:

$$Ln\ (C_t/C_0) = -kt \quad (1)$$

where C_t represents 4-NP concentration at a given time, C_0 denotes a starting 4-NP concentration, and k represents the rate constant of 4-NP reduction by CuCF meshes. The plot of

$Ln(C_t/C_0)$ vs. t is then compiled in Figure 7d, and these data points are well fit by the linear regression, suggesting that the 4-NP reduction by these CuCF meshes can be interpreted properly using the pseudo-first order kinetic model. Corresponding k values for CFM, CFNM and CFCM, were 0.018, 1.56 and 2.46 min^{-1}, respectively. While CFM was also capable of reducing 4-NP to 4-AP, the catalytic activity of CFM seemed much lower than CFNM and CFCM. As CuCF was formed by the coordination of Cu and carboxylates, these CuCF meshes were all comprised of the cluster of Cu–O. Nonetheless, CFNM and CFCM apparently exhibited much higher activities towards the catalytic reduction of 4-NP.

Since catalytic activities would be associated with surface characteristics of catalysts, the relatively faster reduction kinetics by CFNM, and even CFCM, might be related to their surficial properties. As revealed earlier, nanostructures afforded by CuCF, CuCF–NH_2 and CuCF–COOH were significantly distinct, leading to different surface areas, which might influence their catalytic activities. Nevertheless, even though CFM exhibited a slightly higher surface area of 30 m^2/g, the surface areas of CFNM and CFCM (25 and 23 m^2/g, respectively) were actually not significantly lower than that of CFM. Moreover, CFCM, possessing the lowest surface area among these CuCF meshes, enabled the fastest and most efficient 4-NP reduction, suggesting that the surface area was not the main factor affecting catalytic activities of 4-NP in these CuCF meshes.

On the other hand, since 4-NP reduction involves reactions between active sites of catalysts and 4-NP, interactions between 4-NP and CuCF meshes might be critical. As 4-NP contains the nitro group (i.e., NO_2), the N atom would be relatively electron-deficient, whereas the O atom would be more electron-rich, affording $O{=}N^{+}{-}O^{-}$ as the inset displayed in Figure 7a. Therefore, the electrostatic interaction between 4-NP, and CuCF meshes might influence reduction of 4-NP. As revealed earlier, CFNM possessed the amine group and seemed to exhibit relatively positive surface charges, which might increase affinities of 4-NP towards CFNM, thereby improving 4-NP reduction.

Moreover, CFCM might also exhibit affinities towards 4-NP, as CFCM seemed to show a negative surface charge, which would attract the nitro group of 4-NP, thereby leading to the relatively high reduction efficiency of 4-NP. In addition to electrostatic attraction, the aromatic ring of 4-NP is comprised of π electrons, which could also exhibit affinities towards the aromatic ring of CuCF, and the nitro group (acting as an electron-drawing group) is reported to further enhance the π-π interaction, facilitating adsorption [44]. Moreover, since CFCM is comprised of carboxyl groups, these carboxyl groups might enable even stronger affinities of CFCM towards 4-NP through multiple mechanisms [45]. Adebayo et al. also found that the OH group of CuCF–COOH could interact with the OH group of 4-NP through hydrogen bonding [45], whereas the aromatic ring of 4-NP might also interact with the OH group of CuCF–COOH through the donor–acceptor interaction [45]. These affinities and favorable interactions between CFCM and 4-NP might enable CFCM to exhibit much higher efficiencies and faster kinetics for 4-NP reduction.

2.3. Activation Energy (E_a) of 4-NP Reduction by CuCF Meshes

For examining CuCF meshes in the reduction of 4-NP, reduction experiments of 4-NP using CuCF meshes were investigated at various temperatures, as shown in Figure S8, for calculating activation energy (E_a) as follows:

$$\ln k = \ln A - \left(\frac{E_a}{RT}\right) \quad (2)$$

Figure S8 showed the plots of $\ln k$ vs. $1/T$, and the corresponding E_a values for CFM, CFNM and CFCM were 85.0, 28.4 and 28.1 kJ/mol. This validates that CuCF meshes with functional groups (both the amine and carboxyl group) would considerably enhance catalytic 4-NP reduction, possibly owing to higher affinities between 4-NP and these CuCF meshes. For further examining the competitiveness of CuCF meshes, Table 1 summarizes E_a values of 4-NP reduction by CuCF meshes, and other reported catalysts, including noble metal catalysts (e.g., Pt, Au, Ag) and other transition metals, especially Cu. Nevertheless,

CFNM and CFCM both exhibited much lower E_a values than most of the noble metal catalysts [46–52], as well as other Cu/Co/Ni-containing catalysts [53–57], revealing the exceptional advantages of functionalized CuCF meshes.

Table 1. E_a of CuCF meshes and other catalysts in reducing 4-NP.

Catalyst	E_a (kJ/mol)	Ref.
CuCF mesh	85.0	This work
CuCF-NH_2 mesh	28.4	
CuCF-COOH mesh	28.1	
NiY	105	[46]
PtY	136	
CoY	60	
PtNiY	119	
PtCoY	55	
Pt NPs	40	[47]
Magnetic Au-NP	51	[48]
PS-PEGMA-Ag	62	[49]
Cu^{2+}	74	[50]
Ag^{+}	173.1	
$AuCl_4^{-}$	32.6	
Co^{2+}	34.7	
Ni^{2+}	216.4	
Cu-Co/N	53.21	[51]
Ag/Cu	82.7	[52]
$CuFe_2O_4$	44.091	[53]
$Cu_{60}Ni_{40}$–CeO_2	39.695	[54]
Cu/Cu_2O/rGO	24.94	[55]
Cu-APTES@Fe_3O_4	50.5	[56]
$Cu_{2-x}Se$/rGO/PVP	49.05 ± 1.70	[57]
$Cu_{2-x}Se$/PVP	86.47 ± 1.22	
rGO/PVP	77.32 ± 1.60	

2.4. Recyclability of CuCF Meshes, and Reductive Mechanism

As CFCM demonstrated a very promising catalytic activity for 4-NP reduction with fast kinetics and a significantly lower E_a, CFCM was then also investigated for its recyclability for 4-NP reduction. Figure 7e presents 4-NP reduction over consecutive multiple cycles using the spent CFCM, which could remain at consistent efficiency for reducing 4-NP. While k was marginally dropped (from 2.46 to 2.40 min^{-1}), this variation could be associated with the presence of intermediates of $NaBH_4$, which would interfere with reactions between 4-NP and CFCM. The concentration of leached Cu from CFCM in the end of the reusability test over five cycles was further analyzed by an inductively coupled plasma mass spectrometer. The detected concentration for Cu was 0.02 mg/L, which was considerably lower than the dosage of CFCM used in the experiment (i.e., 70 mg/L), suggesting that the leached Cu from CFCM was insignificant. On the other hand, in the used CFCM, the special morphologies of bundles covered on the mesh could still be observed (Figure S9), indicating that the morphology of CFCM was not influenced significantly. The XRD pattern of the used CFCM (Figure S10a) could still be indexed properly with several

signature peaks of CuBTEC. In addition, the used CFCM still exhibited a noticeable amount of N_2 sorption with a hysteresis loop as CFCM still retained the mesoporous structure, as displayed in the inset of Figure S10b. These results demonstrate that CFCM was certainly a durable and efficient catalyst in 4-NP reduction.

The used CFCM had also been investigated by XPS, and its core-level Cu2p and O1s are displayed in Figure S10c,d. In particular, the Cu2p spectrum of used CFCM remained similar to that of pristine CFCM, as two dominant peaks of Cu^{2+} were retained at 933.5 and 953.4 eV [3]. On the other hand, the O1s spectrum of the used CFCM also consisted of a noticeable fraction of Cu–O, in which Cu^{2+} was present [39]. These results suggest that the used CFCM possessed the coordination between Cu and the carboxylate ligand, which would enable it to exhibit consistent catalytic activities over multiple cycles of 4-NP.

Nevertheless, the peak intensities of Cu^{2+} satellite peaks (939.5, 943.3 and 962.7 eV), owing to an unfilled Cu 3 d^9 shell as a result of the presence of CuO [58], seemed to vary slightly after the recyclability test. This also inferred that Cu–O species might be slightly altered during 4-NP reduction, as Cu–O would be the active site.

In view of these analyses, the plausible process in 4-NP reduction using CFCM is illustrated in Figure 8. At the start, $NaBH_4$ might react with the Cu–O cluster of CuCF to generate H_2 molecules [59,60], which might donate electrons to the Cu–O cluster temporarily. After 4-NP is drawn to approach the Cu–O cluster on the CuCF surface, 4-NP would then receive electrons, and incorporate with H+ in aqueous solutions to become 4-AP [61,62]. Eventually, 4-AP would be released from CuCF and returned to the solution.

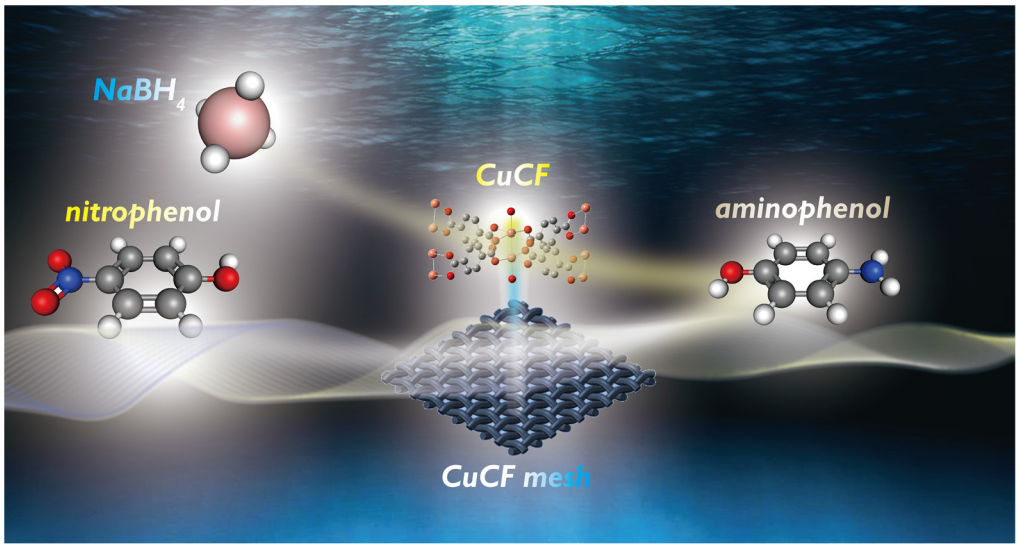

Figure 8. Illustration of 4-NP conversion to 4-AP by CuCF mesh in the presence of $NaBH_4$.

On the other hand, as CFCM exhibited promising activity for the batch-type experiment of 4-NP reduction, it would be interesting to investigate 4-NP reduction by using CFCM as a filter, allowing filtration-type catalytic reactions. Indeed, a piece of CFCM (2.3 cm × 2.3 cm) was placed on the mouth of a glass bottle, and a plastic syringe containing a mixture of 4-NP and $NaBH_4$ solution was vertically placed on the piece of CFCM, as displayed in Figure S11a. After gradually pushing the syringe, the filtered solution was then accumulated in the bottom of the bottle, as shown in Figure S11b. One can note that the original yellowish color of 4-NP had become colorless after filtration. The corresponding UV-Vis spectrum of this colorless solution revealed that the 4-NP at 400 nm had almost disappeared, and converted to 4-AP, demonstrating that CFCM can also be employed for filtration-type catalytic reactions.

2.5. The Reduction Reaction of Nitrophenol Isomers

In addition to 4-NP, 2-NP and 3-NP are also intensely concerning as NP isomers [63]; thus, the reduction of 2-NP and 3-NP by these CuCF meshes was then studied. Figure 9a displays the UV-Vis spectra of 2-NP in the presence of $NaBH_4$ and CFCM at increasing reaction times, in which the signature peak of 2-NP located at 417 nm gradually decreased, and almost disappeared after 180 s. This demonstrates that CFCM can be utilized for 2-NP reduction. In addition, Figure 9b displays 2-NP in the presence of a pristine Cu mesh and $NaBH_4$; however, the concentration of 2-NP remained almost unchanged, indicating that the pristine Cu mesh could not reduce 2-NP. When CFM was then used, 2-NP could be noticeably decreased; nevertheless, the reduction efficiency seemed very limited, and its corresponding k was merely 0.24 min^{-1}. Once CFNM was employed, 2-NP was noticeably reduced, and its kinetics seemed considerably accelerated with a much higher $k = 1.2$ min^{-1}. On the other hand, CFCM could enable a much higher rate constant of 2-NP reduction, of $k = 2.1$ min^{-1}.

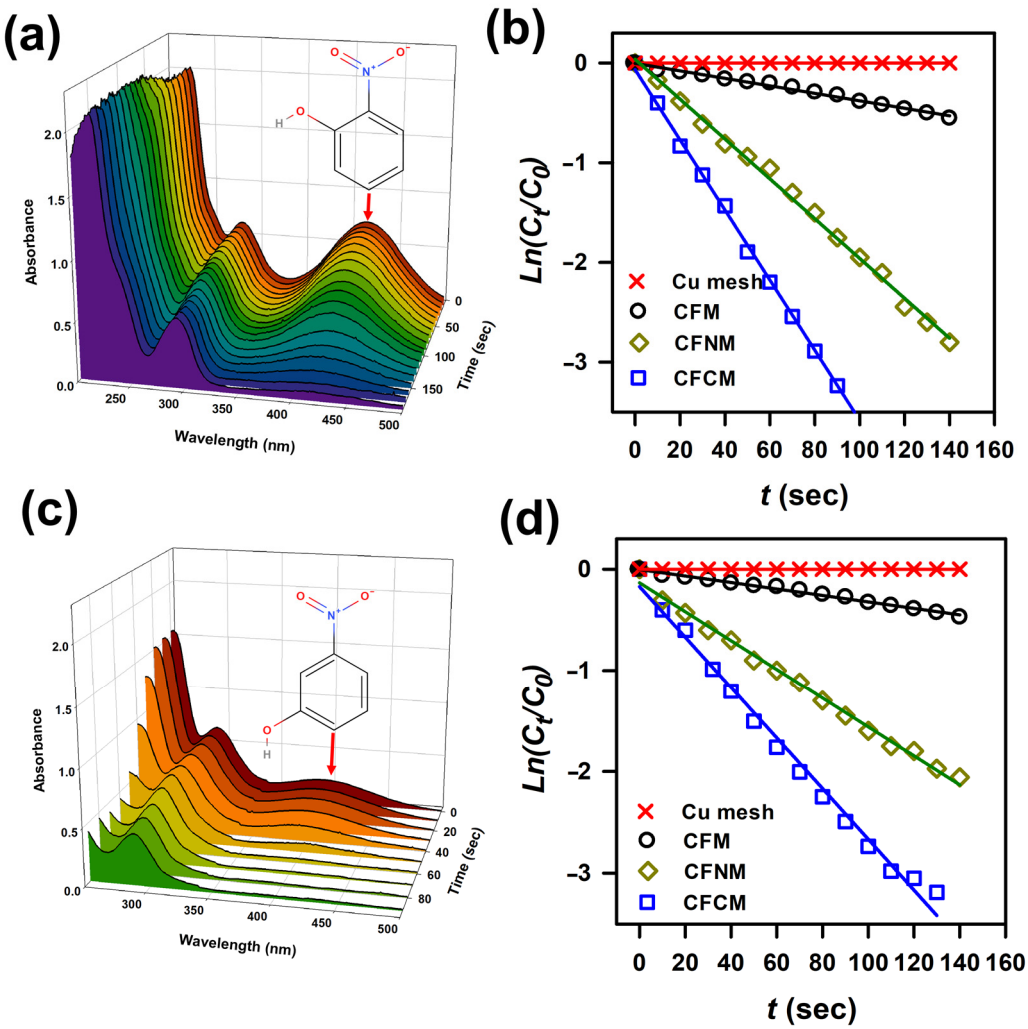

Figure 9. (**a**) Time-dependent UV-Vis absorption spectra of 2-NP during reduction using CFCM; (**b**) pseudo-first order plots of 2-NP reduction by various meshes; (**c**) time-dependent UV-Vis absorption spectra of 3-NP during reduction using CFCM; (**d**) pseudo-first order plots of 4-NP reduction by various meshes.

On the other hand, Figure 9c displays the reduction of another isomer, 3-NP, in the presence of $NaBH_4$ and CFCM at different reaction times, in which the characteristic peak of 3-NP located at 417 nm rapidly decreased, and almost vanished after 90 s. This also

validated that CFCM can be applied for 3-NP reduction. Furthermore, Figure 9d shows 3-NP in the presence of pristine Cu mesh and $NaBH_4$; nevertheless, the concentration of 3-NP was almost the same, signifying that the pristine Cu mesh itself could not reduce 3-NP. Once CFM was then adopted, 3-NP was slightly decreased; however, the reduction efficiency was also relatively low, and its k was merely 0.18 min^{-1}. When CFNM was employed, 3-NP was noticeably reduced, and its kinetics were notably expedited with a higher k = 0.84 min^{-1}. Moreover, CFCM could also lead to a much higher rate constant of 3-NP reduction as k = 1.5 min^{-1}.

These results suggest that functionalized CFCM and CFNM could also exhibit much higher reduction efficiencies for 2-NP and 3-NP. These results were similar to the observation of 4-NP reduction by these meshes, suggesting that the functionality of CuCF meshes was validated to enhance reduction of 2-NP and 3-NP, possibly owing to the higher affinities between 2-NP/3-NP and functional groups of CuCF meshes, as 2-NP/3-NP is actually comparable to 4-NP with the same functional groups.

2.6. CuCF Meshes for MB and MO Reduction/Hydrogeneration

Aside from NPs, CuCF meshes were then also investigated for nitrogen-containing dyes, which can be decolorized via catalytic reduction/hydrogeneration [64,65]. In particular, methylene blue (MB) is a widely employed blue dye, and a medication for treating methemoglobinemia. MB can be decolorized through catalytic hydrogenation, converting MB to leuco-methylene blue [64,65].

Figure 10a shows the UV-Vis spectra of MB by CFCM and $NaBH_4$ at increasing times, and how the main bands of MB at 600 and 660 nm continuously dropped, and then almost ceased in 70 s. This demonstrates that CFCM could be utilized for MB decolorization via hydrogenation. Moreover, Figure 10b reveals MB in the presence of the pristine Cu mesh, and $NaBH_4$; however, the concentration of MB remained almost constant, indicating that the pristine Cu mesh was not capable of hydrogenating MB. Subsequently, when CFM was then used, the concentration of MB could be gradually decreased in 140 s with a k = 0.78 min^{-1}, indicating that CFM was also capable of hydrogenating MB. In the case of CFNM, the decolorization of MB proceeded slightly slower and less efficiently, leading to a much higher k = 0.54 min^{-1}. Once CFCM was adopted, MB could be decolorized even faster, and much more effectively, leading to a significantly higher k = 1.14 min^{-1}. These results unveil that CuCF meshes were all capable of hydrogenating MB for decolorization, possibly because these CuCF meshes were comprised of Cu-O, which is validated to hydrogenate the MB molecule [66], causing decolorization. CFNM was shown to be relatively positively charged, and thus the affinity between the cationic MB and CFNM might become much less, or even mutual repulsion might be slightly higher, thereby leading to less efficient MB hydrogenation. In contrast, CFCM appeared to be the most efficient for decolorizing MB, probably because MB is a cationic molecule, which might exhibit a higher affinity towards the negatively charged CFCM, leading to the faster reaction kinetics. Table 2 further lists the rate constants of MB decolorization by CFCM and other reported catalysts, and CFCM certainly showed a much higher rate constant than other values in the literature, even compared to Pt and Ag, revealing the advantage of CFCM for MB decolorization.

As CFCM exhibited promising activity for the batch-type experiment of MB decolorization, it was then useful to study MB decolorization by using CFCM as a filter for filtering-type catalytic processes. A piece of CFCM was placed on a glass bottle (Figure S12a), and a syringe containing a mixture of MB and $NaBH_4$ solution was placed on the piece of CFCM. After pressing the syringe, and the filtered solution was then collected in the bottom of the bottle, as shown in Figure S12b. The original blueish color of MB became colorless after filtration. The corresponding UV-Vis spectrum of this colorless solution revealed that the MB at 660 nm had almost disappeared, and also converted to LMB, demonstrating that CFCM can be also employed for filtration-type catalytic decolorization applications.

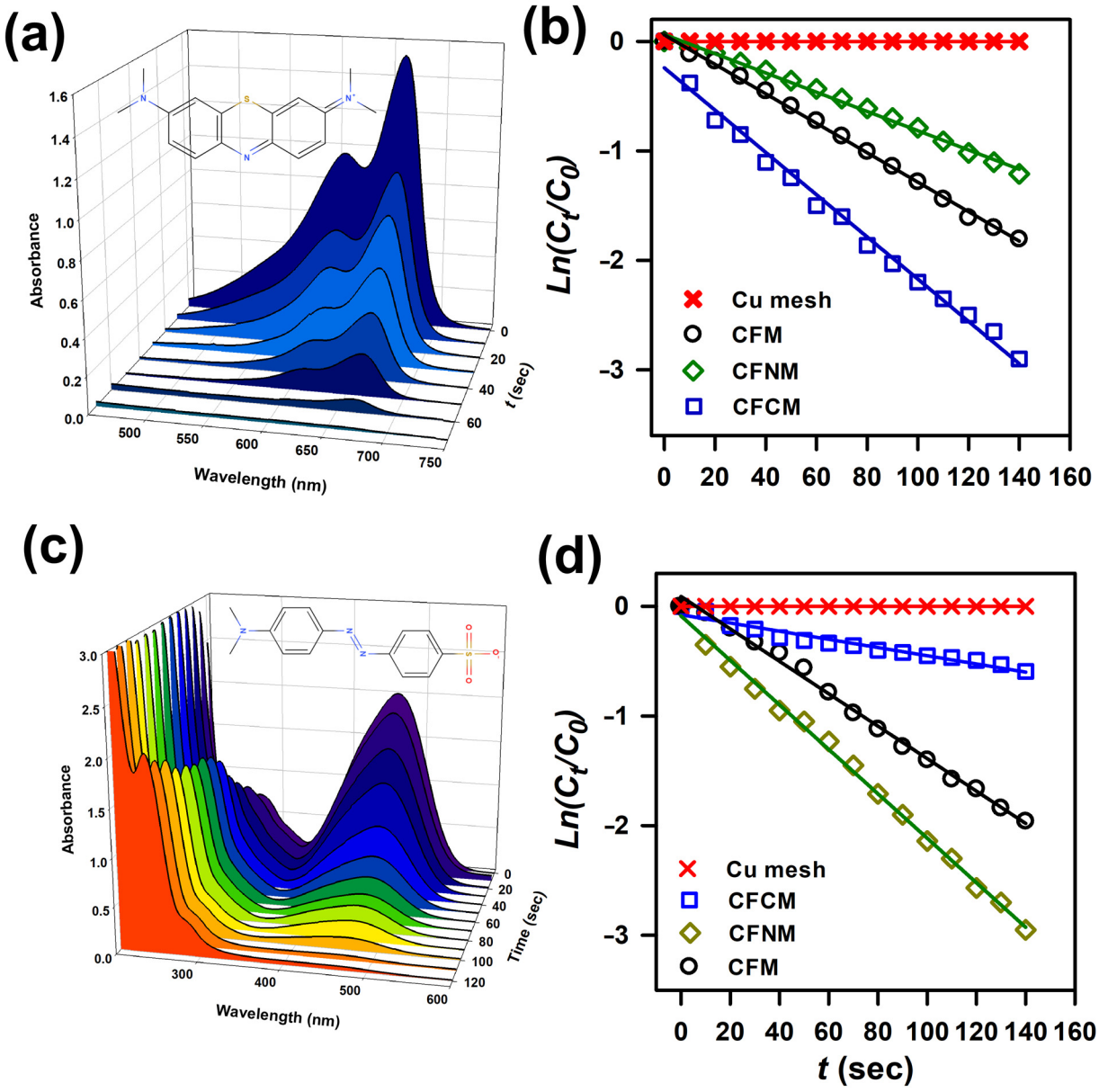

Figure 10. (**a**) Time-dependent UV-Vis absorption spectra of MB during reduction using CFCM; (**b**) pseudo-first order plots of 2-NP reduction by various meshes; (**c**) time-dependent UV-Vis absorption spectra of 3-NP during reduction using CFNM; (**d**) pseudo-first order plots of 4-NP reduction by various meshes.

Table 2. Comparison of rate constant (*k*) of CFCM and different reported catalysts for the reduction of MB.

Material	k (min^{-1})	Citation
CFCM	**1.14**	**This work**
pNAC7	0.80	[67]
Platinum particles	0.03	[68]
Mg/Al-hydroxide@Gold	0.84	[69]
Mg/Al/Ce-hydroxide@Gold	1.80	
Mg/Al/Ce-hydroxide	0.30	

Table 2. *Cont.*

Material	k (min^{-1})	Citation
Silver particles	0.20	[70]
Cotton@Silver particles	0.48	[71]
Palladium/Silica	1.43	[72]
Ce/Zr@Cu^0	0.17	[73]
CA@Cu^0	0.083	
CA-Ce/Ze@ Cu^0	0.096	
CuNi@CP	0.026	[74]
Cu@CC	0.246	
Ni	0.12	[75]
Ni@Cu	0.52	
Ni@Cu@Pd	7.2	
Cu-Ni	0.38	
Porous Cu	0.81	

In addition to the cationic MB, it is interesting to explore these CuCF meshes for the decolorization of anionic dye. Thus, an extensively used anionic dye, methyl orange (MO), was selected and investigated. Figure 10c shows MO in the presence of $NaBH_4$ and CFNM at different reaction times, in which the characteristic peak of MO at 465 nm quickly decreased over 120 s, and a peak corresponding to the derivatives from decomposition of MO at 240 nm gradually raised up, suggesting that CuCF meshes were capable of reducing MO [76,77]. Figure 10d also reveals MO in the presence of the pristine Cu mesh and $NaBH_4$; however, the concentration of MO was barely changed, demonstrating that the pristine Cu mesh could not reduce MO. Next, as CFM was then employed, the concentration of MO progressively decreased within 120 s with a $k = 0.78\ min^{-1}$, indicating that CFM could also hydrogenate MO. In the case of CFNM, the decolorization of MO proceeded noticeably faster, resulting in a much higher $k = 1.2\ min^{-1}$. Once CFCM was employed, the decolorization of MO seemed to proceed slowly, leading to a notably smaller $k = 0.24\ min^{-1}$. These results unveil that CuCF meshes were all capable of hydrogenating MO for decolorization, as the Cu-O cluster in these CuCF meshes could catalytically hydrogenate the azo group of MO, and cause cleavage of MO, leading to decolorization of MO [76,77]. Moreover, as CFNM was shown to be relatively positively charged, and the affinity between the cationic MO and CFNM might grow stronger, or the mutual revulsion might be less, thereby resulting in more efficient MO reduction. Conversely, CFCM appeared as the least efficient for decolorizing MO, possibly because of a lower affinity of MO towards the negatively charged CFCM, leading to slower reaction kinetics. Table 3 summarizes a list of rate constants of MO reduction by CFNM and other reported catalysts; CFNM certainly exhibited a much higher rate constant than most of the reported values, even from noble metal catalysts (e.g., Pt, and Ag), revealing the high competitiveness of CFCM for MO decolorization.

Next, a piece of CFNM was placed on a glass bottle, and a syringe containing a mixture of MO and $NaBH_4$ solution was placed on the piece of CFNM (Figure S13a). After pushing the syringe, and the filtered solution was then accumulated in the bottom of the bottle, as shown in Figure S13b. The original orange color of MO became colorless after filtration. The corresponding UV-Vis spectrum of this colorless solution revealed that the MO at 465 nm had almost vanished, and a peak at 240 nm raised up, validating that CFNM can also be employed for filtration-type catalytic decolorization applications.

Table 3. Comparison of rate constant (*k*) of CFNM and different reported catalysts for the reduction of MO.

Catalyst	k (min^{-1})	Ref.
CFNM	**1.2**	**This work**
$CuVOS@SiO_2$	0.411	[78]
CuO nanosheets	0.0069	[79]
PtNPs	4.145	[80]
PdNPs	0.0125	
AuNPs	0.0067	
AgNPs	0.00007	
CuSnOS@AC-0.30 mL	0.826	[81]
$Au@Cu_2O$ NCs	0.299	[82]
$Au@Cu_2O$-Ag NCs	1.081	

3. Materials and Methods

3.1. Materials

The chemicals employed in this study were commercially available, and employed directly. Cu mesh (#200 mesh) was purchased from Mei-Syun Enterprise LTD (Taichung City, Taiwan). Copper nitrate ($Cu(NO_3)_2$), benzene-1,4-dicarboxylic acid (BDC), 2-aminobenzene-1,4-dicarboxylic acid (BDC-NH_2), methyl orange (MO) and 1,2,4,5-benzenetetracarboxylic acid (BTEC), methylene blue (MB) were obtained from Sigma-Aldrich (St. Louis, MO, USA). 4-NP, 2-NP and 3-NP were received from Acros Organics (Branchburg, NJ, USA). Sodium borohydride ($NaBH_4$), and N,N-dimethylacetamide were received from Showa Chemicals (Minato City, Tokyo, Japan).

3.2. Preparation of CuCF Mesh Catalysts

Fabrication of CuCF meshes through the single-step procedure is depicted schematically in Figure 1a. Initially, Cu mesh (5 cm × 5 cm) was cleansed with hydrochloric acid (5 M) for 15 min, followed by rinsing with DI water. Next, Cu mesh and a carbon electrode acted as an anode and a cathode, respectively. A carboxylate ligand was then dissolved in 125 mL of N, N-dimethylacetamide to form an electrolyte solution (5 mM). The anodizing fabrication of CuCF would be executed (5 V for a half of hour) at 25 °C. Subsequently, the resulting CuCF mesh was cleaned by DI water and dried to produce a CuCF mesh.

3.3. Characterization of CuCF Meshes

Appearances of CuCF meshes were visualized by scanning electronic microscopy (ZEISS Sigma 500 VP, Ostalbkreis, Germany). Crystalline structures of Cu meshes were obtained using a diffractometer, whereas the chemistry of these Cu meshes was analyzed by X-ray photoelectron spectroscopy (XPS). The textural properties of Cu meshes were analyzed by a BET surface area analyzer (Anton Paar, Graz, Austria), whereas surface charges of meshes were detected by a zetasizer (Malvern, Malvern, UK).

3.4. Reduction of NCPCs Using CuCF Meshes

Reduction of NCPCs using CuCF meshes was conducted firstly by batch-type experiments. In the case of 4-NP, a 4-NP solution (3.6 mM) and a $NaBH_4$ solution (4.2 M) were obtained. Subsequently, 2.5 cm^3 of the aforementioned 4-NP solution was added to 47.5 cm^3 of DI water, followed by 0.2 cm^3 of the aforementioned $NaBH_4$ solution. Next, 3.5 mg of CuCF mesh was then immediately placed into the 4-NP/$NaBH_4$ mixture at a pre-set temperature to initiate the catalytic reduction experiment. Then, spectral variation of the reduction of 4-NP was then measured using a spectrophotometer (JASCO, Tokyo, Japan). The variation of 4-NP was quantified through measurement of the absorbance

at 400 nm at various reaction times. Variations of 2-NP and 3-NP concentrations were also determined using the same protocol, whereas variations of MB and MO concentrations were identified by monitoring spectral variation in the ranges of 150~700 nm and 200~600 nm, separately. The concentration of Cu leached out from CFCM was determined using inductively coupled plasma mass spectrometry (ICP-MS) (ICP-MS ELEMENT™ GD PLUS GD, Thermo Fisher, Branchburg, NJ, USA).

4. Conclusions

In this study, hierarchically structured catalysts comprised of copper carboxylate frameworks (CuCF) were fabricated. Specifically, a CuCF mesh functionalized with NH_2 (CFNM), a CuCF mesh functionalized with COOH (CFCM), and a pristine CuCF mesh (CFM) were prepared. While the pristine Cu mesh was almost incapable of reducing 4-NP, these CuCF meshes could all catalyze 4-NP reduction. In particular, CFCM appeared as the most efficient mesh for catalyzing 4-NP with a much higher rate constant, followed by CFNM, and then CFM. This was possibly because the affinity between 4-NP and CFCM seemed much higher owing to stronger hydrogen bonding between the carboxyl group of CFCM and 4-NP, as well as enhanced π-π interaction. CFCM also showed a significantly lower E_a in comparison to the reported values. CFCM could also be employed over many consecutive cycles, and for convenient filtration-type 4-NP reduction. These CuCF meshes can also be employed for decolorization of MB and MO dyes via catalytic hydrogenation. Interestingly, CFCM was found to be the most efficient Cu mesh among these three Cu meshes for MB decolorization, possibly owing to the higher affinity between the anionic CFCM and the cationic MB. On the other hand, CFNM exhibited a relatively high rate constant for decolorizing MO among these three Cu meshes, probably because of the strong affinity between the cationic CFNM, and the anionic MO. These features validate that CuCF meshes are conveniently prepared and highly efficient hierarchically heterogeneous catalysts for the reduction of nitrogen-containing contaminants, and functional groups of CuCF meshes can further enhance their catalytic behaviors.

Supplementary Materials: The following supporting information can be downloaded at: https://www.mdpi.com/article/10.3390/catal12070765/s1, Figure S1: SEM images of the pristine Cu mesh; Figure S2; IR analyses of ligands. Figure S3: XPS of pristine Cu mesh: (a) full spectrum, and (b) Cu2p; Figure S4: Pore size distributions of CF meshes; Figure S5: Thermogravimetric analyses of CuCF meshes in N_2; Figure S6: UV-Vis spectra of 4-NP with and without $NaBH_4$, and 4-AP; 4-NP (without $NaBH_4$) in the presence of pristine Cu mesh, 4-NP (without $NaBH_4$) in the presence of CFM, 4-NP (without $NaBH_4$) in the presence of CFNM, 4-NP (without $NaBH_4$) in the presence of CFCM; Figure S7: UV-Vis spectra of 4-NP with $NaBH_4$ in the presence of pristine Cu mesh; Figure S8: 4-NP reduction plots of Ln (Ct/C0) vs t, and plots of Ln K vs. 1/t of by (a,d) CFM, (b,e) CFNM, and (c,f) CFCM; Figure S9: SEM image of the used CFCM; Figure S10: (a) XRD, (b) N_2 sorption isotherm, and XPS analyses of used CFCM: (c) Cu2p, and (d) O1s core-level spectra; Figure S11: Demonstration of filtration-type 4-NP reduction by CFCM; Figure S12: Demonstration of filtration-type MB reduction by CFCM; Figure S13: Demonstration of filtration-type MO reduction by CFNM.

Author Contributions: Data curation, writing—original draft preparation, P.-H.M., N.N.H. and S.G.; data curation, visualization, investigation, J.-Y.L. and E.K.; writing—reviewing and editing, F.-Y.Y. and G.L.; data curation, writing—original draft preparation, F.G. and K.-Y.A.L. All authors have read and agreed to the published version of the manuscript.

Funding: This project has been supported by Abadan University of Medical Sciences (Iran) under Contract No. 1400RCEC1426.

Data Availability Statement: The data presented in this study are available in this study and Supplementary Materials.

Conflicts of Interest: The authors declare no conflict of interest.

References

1. Patterson, J.W. *Industrial Wastewater Treatment Technology*, 2nd ed.; Butterworth Publishers: Stoneham, MA, USA, 1985.
2. Godain, A.; Spurr, M.W.A.; Boghani, H.C.; Premier, G.C.; Yu, E.H.; Head, I.M. Detection of 4-Nitrophenol, a Model Toxic Compound, Using Multi-Stage Microbial Fuel Cells. *Front. Environ. Sci.* **2020**, *8*, 5. [CrossRef]
3. Wi-Afedzi, T.; Kwon, E.; Tuan, D.D.; Lin, K.-Y.A.; Ghanbari, F. Copper hexacyanoferrate nanocrystal as a highly efficient non-noble metal catalyst for reduction of 4-nitrophenol in water. *Sci. Total Environ.* **2020**, *703*, 134781. [CrossRef]
4. Andrew Lin, K.-Y.; Hsieh, Y.-T. Copper-based metal organic framework (MOF), HKUST-1, as an efficient adsorbent to remove p-nitrophenol from water. *J. Taiwan Inst. Chem. Eng.* **2015**, *50*, 223–228. [CrossRef]
5. Tafesh, A.M.; Weiguny, J. A review of the selective catalytic reduction of aromatic nitro compounds into aromatic amines, isocyanates, carbamates, and ureas using CO. *Chem. Rev.* **1996**, *96*, 2035–2052.
6. Hammud, H.H.; Traboulsi, H.; Karnati, R.K.; Hussain, S.G.; Bakir, E.M. Hierarchical Graphitic Carbon-Encapsulating Cobalt Nanoparticles for Catalytic Hydrogenation of 2,4-Dinitrophenol. *Catalysts* **2022**, *12*, 39. [CrossRef]
7. Panda, J.; Biswal, S.P.; Jena, H.S.; Mitra, A.; Samantray, R.; Sahu, R. Role of Lewis Acid Metal Centers in Metal–Organic Frameworks for Ultrafast Reduction of 4-Nitrophenol. *Catalysts* **2022**, *12*, 494. [CrossRef]
8. Ribeiro, A.P.C.; Santos, B.M.; Faustino, R.F.C.; Pombeiro, A.J.L.; Martins, L.M.D.R.S. C-Heterogenized Re Nanoparticles as Effective Catalysts for the Reduction of 4-Nitrophenol and Oxidation of 1-Phenylethanol. *Catalysts* **2022**, *12*, 285. [CrossRef]
9. Scurti, S.; Allegri, A.; Liuzzi, F.; Rodríguez-Aguado, E.; Cecilia, J.A.; Albonetti, S.; Caretti, D.; Dimitratos, N. Temperature-Dependent Activity of Gold Nanocatalysts Supported on Activated Carbon in Redox Catalytic Reactions: 5-Hydroxymethylfurfural Oxidation and 4-Nitrophenol Reduction Comparison. *Catalysts* **2022**, *12*, 323. [CrossRef]
10. Shultz, L.R.; Feit, C.; Stanberry, J.; Gao, Z.; Xie, S.; Anagnostopoulos, V.A.; Liu, F.; Banerjee, P.; Jurca, T. Ultralow Loading Ruthenium on Alumina Monoliths for Facile, Highly Recyclable Reduction of p-Nitrophenol. *Catalysts* **2021**, *11*, 165. [CrossRef]
11. Krishna, R.; Fernandes, D.M.; Domingos, V.F.; Ribeiro, E.S.; Gil, J.C.; Dias, C.; Ventura, J.; Freire, C.; Titus, E. Reduction of 4-nitrophenol to 4-aminophenol using a novel Pd@NixB–SiO_2/RGO nanocomposite: Enhanced hydrogen spillover and high catalytic performance. *RSC Adv.* **2015**, *5*, 60658–60666. [CrossRef]
12. Kuroda, K.; Ishida, T.; Haruta, M. Reduction of 4-nitrophenol to 4-aminophenol over Au nanoparticles deposited on PMMA. *J. Mol. Catal. A Chem.* **2009**, *298*, 7–11. [CrossRef]
13. Govindaraju, S.; Arumugasamy, S.K.; Chellasamy, G.; Yun, K. Zn-MOF decorated bio activated carbon for photocatalytic degradation, oxygen evolution and reduction catalysis. *J. Hazard. Mater.* **2022**, *421*, 126720. [CrossRef]
14. Rego, R.M.; Kurkuri, M.D.; Kigga, M. A comprehensive review on water remediation using UiO-66 MOFs and their derivatives. *Chemosphere* **2022**, *302*, 134845. [CrossRef]
15. Khan, N.A.; Hasan, Z.; Jhung, S.H. Adsorptive removal of hazardous materials using metal-organic frameworks (MOFs): A review. *J. Hazard. Mater.* **2013**, *244–245*, 444–456. [CrossRef]
16. Li, B.; Zhao, D.; Wang, F.; Zhang, X.; Li, W.; Fan, L. Recent advances in molecular logic gate chemosensors based on luminescent metal organic frameworks. *Dalton Trans.* **2021**, *50*, 14967–14977. [CrossRef]
17. Lv, H.; Zhang, Z.; Fan, L.; Gao, Y.; Zhang, X. A nanocaged cadmium-organic framework with high catalytic activity on the chemical fixation of CO_2 and deacetalization-knoevenagel condensation. *Microporous Mesoporous Mater.* **2022**, *335*, 111791. [CrossRef]
18. Wang, F.; Zhao, D.; Li, B.; Li, W.; Zhang, H.; Pang, J.; Fan, L. Compositional Engineering of Co(II)MOF/Carbon-Based Overall Water Splitting Electrocatalysts: From Synergistic Effects to Structure–Activity Relationships. *Cryst. Growth Des.* **2022**, *22*, 2775–2792. [CrossRef]
19. Kang, X.; Teng, D.; Wu, S.; Tian, Z.; Liu, J.; Li, P.; Ma, Y.; Liang, C. Ultrafine copper nanoparticles anchored on reduced graphene oxide present excellent catalytic performance toward 4-nitrophenol reduction. *J. Colloid Interface Sci.* **2020**, *566*, 265–270. [CrossRef]
20. Chiu, H.-Y.; Wi-Afedzi, T.; Liu, Y.-T.; Ghanbari, F.; Lin, K.-Y.A. Cobalt Oxides with Various 3D Nanostructured Morphologies for Catalytic Reduction of 4-Nitrophenol: A Comparative Study. *J. Water Process Eng.* **2020**, *37*, 101379. [CrossRef]
21. Jiang, D.B.; Liu, X.; Yuan, Y.; Feng, L.; Ji, J.; Wang, J.; Losic, D.; Yao, H.-C.; Zhang, Y.X. Biotemplated top-down assembly of hybrid Ni nanoparticles/N doping carbon on diatomite for enhanced catalytic reduction of 4-nitrophenol. *Chem. Eng. J.* **2020**, *383*, 123156. [CrossRef]
22. Wang, S.; Song, Y.; Jiang, L. Microscale and nanoscale hierarchical structured mesh films with superhydrophobic and superoleophilic properties induced by long-chain fatty acids. *Nanotechnology* **2006**, *18*, 015103. [CrossRef]
23. Guo, Z.; Zheng, X.; Tian, D.; Song, Y.; Zhai, J.; Zhang, X.; Li, W.; Wang, X.; Dou, S.; Jiang, L. Photoelectric cooperative patterning of liquid permeation on the micro/nano hierarchically structured mesh film with low adhesion. *Nanoscale* **2014**, *6*, 12822–12827. [CrossRef] [PubMed]
24. Xiong, J.; Li, A.; Liu, Y.; Wang, L.; Qin, X.; Yu, J. Scalable and hierarchically designed MOF fabrics by netting MOFs into nanofiber networks for high-performance solar-driven water purification. *J. Mater. Chem. A* **2021**, *9*, 21005–21012. [CrossRef]
25. Nanthamathee, C. Effect of Co(II) dopant on the removal of Methylene Blue by a dense copper terephthalate. *J. Environ. Sci.* **2019**, *81*, 68–79. [CrossRef]
26. Zhang, Q.; Muhan, C.; Zhong, L.; Ye, Q.; Jiang, S.; Huang, Z. Highly Effective Removal of Metal Cyanide Complexes and Recovery of Palladium Using Quaternary-Ammonium-Functionalized MOFs. *Molecules* **2018**, *23*, 2086. [CrossRef]

27. Ebrahimi, A.K.; Sheikhshoaie, I.; Mehran, M. Facile synthesis of a new metal-organic framework of copper (II) by interface reaction method, characterization, and its application for removal of Malachite Green. *J. Mol. Liq.* **2017**, *240*, 803–809. [CrossRef]
28. Hu, X.; Tian, X.; Lin, Y.-W.; Wang, Z. Nickel foam and stainless steel mesh as electrocatalysts for hydrogen evolution reaction, oxygen evolution reaction and overall water splitting in alkaline media. *RSC Adv.* **2019**, *9*, 31563–31571. [CrossRef]
29. Gupta, N.K.; Kim, S.; Bae, J.; Kim, K.S. Chemisorption of hydrogen sulfide over copper-based metal–organic frameworks: Methanol and UV-assisted regeneration. *RSC Adv.* **2021**, *11*, 4890–4900. [CrossRef]
30. Gao, L.-L.; Liu, Y.; Lv, X.-Y.; Liu, J.-F.; Hu, T.-P. Crystal Structure and Thermal Behavior of Two New Supramolecular Complexes Templated with 1,2,4,5-Benzenetetracarboxylic Acid. *Int. J. Inorg. Chem.* **2012**, *2012*, 291682. [CrossRef]
31. Surib, N.A.; Kuila, A.; Saravanan, P.; Sim, L.C.; Leong, K.H. A ligand strategic approach with Cu-MOF for enhanced solar light photocatalysis. *New J. Chem.* **2018**, *42*, 11124–11130. [CrossRef]
32. Zhang, Z.; Tao, C.-A.; Zhao, J.; Wang, F.; Huang, J.; Wang, J. Microwave-Assisted Solvothermal Synthesis of UiO-66-NH2 and Its Catalytic Performance toward the Hydrolysis of a Nerve Agent Simulant. *Catalysts* **2020**, *10*, 1086. [CrossRef]
33. Mukaromah, L.; Permana, Y.; Patah, A. Influence of Room-Temperature Ionic Liquids on the Electrosynthesis of CuBDC Type Metal-Organic Frameworks: Crystallite Size and Productivity. *J. Res. Dev. Nanotec.* **2022**, *1*, 1–5. [CrossRef]
34. Shetti, N.P.; Nandibewoor, S.T. Kinetic and Mechanistic Investigations on Oxidation of L-tryptophan by Diperiodatocuprate(III) in Aqueous Alkaline Medium. *Z. Phys. Chem.* **2009**, *223*, 299–317. [CrossRef]
35. Mitchell, C.J.; Yang, G.-R.; Senkevich, J.J. Adhesion aspects of poly(p-xylylene) to SiO_2 surfaces using γ-methacryloxypropy ltrimethoxysilane as an adhesion promoter. *J. Adhes. Sci. Technol.* **2006**, *20*, 1637–1647. [CrossRef]
36. De Sousa, P.V.F.; de Oliveira, A.F.; da Silva, A.A.; Lopes, R.P. Environmental remediation processes by zero valence copper: Reaction mechanisms. *Environ. Sci. Pollut. Res.* **2019**, *26*, 14883–14903. [CrossRef]
37. Rivera-Torrente, M.; Filez, M.; Schneider, C.; van der Feltz, E.C.; Wolkersdorfer, K.; Taffa, D.H.; Wark, M.; Fischer, R.A.; Weckhuysen, B.M. Micro-spectroscopy of HKUST-1 metal-organic framework crystals loaded with tetracyanoquinodimethane: Effects of water on host-guest chemistry and electrical conductivity. *Phys. Chem. Chem. Phys.* **2019**, *21*, 25678–25689. [CrossRef]
38. Wang, Z.; Zhang, Y.; Xiong, H.; Qin, C.; Zhao, W.; Liu, X. Yucca fern shaped CuO nanowires on Cu foam for remitting capacity fading of Li-ion battery anodes. *Sci. Rep.* **2018**, *8*, 6530. [CrossRef]
39. Sun, Y.; Xue, Z.; Liu, Q.; Jia, Y.; Li, Y.; Liu, K.; Lin, Y.; Liu, M.; Li, G.; Su, C.-Y. Modulating electronic structure of metal-organic frameworks by introducing atomically dispersed Ru for efficient hydrogen evolution. *Nat. Commun.* **2021**, *12*, 1369. [CrossRef]
40. Uthappa, U.T.; Sriram, G.; Arvind, O.R.; Kumar, S.; Ho Young, J.; Neelgund, G.M.; Losic, D.; Kurkuri, M.D. Engineering MIL-100(Fe) on 3D porous natural diatoms as a versatile high performing platform for controlled isoniazid drug release, Fenton's catalysis for malachite green dye degradation and environmental adsorbents for Pb2+ removal and dyes. *Appl. Surf. Sci.* **2020**, *528*, 146974. [CrossRef]
41. Wang, Y.-L.; Dai, Y.-M.; Tsai, M.-H. Highly efficient and recyclable Fe_3C/Au@NG catalyst for 4-nitrophenol reduction. *Catal. Commun.* **2021**, *149*, 106251. [CrossRef]
42. Xu, Y.; Shi, X.; Hua, R.; Zhang, R.; Yao, Y.; Zhao, B.; Liu, T.; Zheng, J.; Lu, G. Remarkably catalytic activity in reduction of 4-nitrophenol and methylene blue by Fe_3O_4@COF supported noble metal nanoparticles. *Appl. Catal. B* **2020**, *260*, 118142. [CrossRef]
43. Wi-Afedzi, T.; Yeoh, F.-Y.; Yang, M.-T.; Yip, A.C.K.; Lin, K.-Y.A. A comparative study of hexacyanoferrate-based Prussian blue analogue nanocrystals for catalytic reduction of 4-nitrophenol to 4-aminophenol. *Sep. Purif. Technol.* **2019**, *218*, 138–145. [CrossRef]
44. Dhorabe, P.T.; Lataye, D.H.; Ingole, R.S. Removal of 4-nitrophenol from aqueous solution by adsorption onto activated carbon prepared from *Acacia glauca* sawdust. *Water Sci. Technol.* **2015**, *73*, 955–966. [CrossRef] [PubMed]
45. Adebayo, M.A.; Areo, F.I. Removal of phenol and 4-nitrophenol from wastewater using a composite prepared from clay and *Cocos nucifera* shell: Kinetic, equilibrium and thermodynamic studies. *Resour. Environ. Sustain.* **2021**, *3*, 100020. [CrossRef]
46. El-Bahy, Z.M. Preparation and characterization of Pt-promoted NiY and CoY catalysts employed for 4-nitrophenol reduction. *Appl. Catal. A* **2013**, *468*, 175–183. [CrossRef]
47. Wunder, S.; Polzer, F.; Lu, Y.; Mei, Y.; Ballauff, M. Kinetic Analysis of Catalytic Reduction of 4-Nitrophenol by Metallic Nanoparticles Immobilized in Spherical Polyelectrolyte Brushes. *J. Phys. Chem. C* **2010**, *114*, 8814–8820. [CrossRef]
48. Chang, Y.C.; Chen, D.H. Catalytic reduction of 4-nitrophenol by magnetically recoverable Au nanocatalyst. *J. Hazard. Mater.* **2009**, *165*, 664–669. [CrossRef]
49. Lu, Y.; Mei, Y.; Walker, R.; Ballauff, M.; Drechsler, M. 'Nano-tree'—Type spherical polymer brush particles as templates for metallic nanoparticles. *Polymer* **2006**, *47*, 4985–4995. [CrossRef]
50. Wu, X.-Q.; Wu, X.-W.; Shen, J.-S.; Zhang, H.-W. In situ formed metal nanoparticle systems for catalytic reduction of nitroaromatic compounds. *RSC Adv.* **2014**, *4*, 49287–49294. [CrossRef]
51. Li, X.; Yan, X.; Hu, X.; Feng, R.; Zhou, M.; Wang, L. Hollow Cu-Co/N-doped carbon spheres derived from ZIFs as an efficient catalyst for peroxymonosulfate activation. *Chem. Eng. J.* **2020**, *397*, 125533. [CrossRef]
52. Sharma, M.; Hazra, S.; Basu, S. Synthesis of heterogeneous Ag-Cu bimetallic monolith with different mass ratios and their performances for catalysis and antibacterial activity. *Adv. Powder Technol.* **2017**, *28*, 3085–3094. [CrossRef]
53. Dey, C.; De, D.; Nandi, M.; Goswami, M.M. A high performance recyclable magnetic $CuFe_2O_4$ nanocatalyst for facile reduction of 4-nitrophenol. *Mater. Chem. Phys.* **2020**, *242*, 122237. [CrossRef]

54. Kohantorabi, M.; Gholami, M.R. Kinetic analysis of the reduction of 4-nitrophenol catalyzed by CeO_2 nanorods-supported CuNi nanoparticles. *Ind. Eng. Chem. Res.* **2017**, *56*, 1159–1167. [CrossRef]
55. Xie, Y.; Liu, B.; Li, Y.; Chen, Z.; Cao, Y.; Jia, D. Cu/Cu_2O/rGO nanocomposites: Solid-state self-reduction synthesis and catalytic activity for p-nitrophenol reduction. *New J. Chem.* **2019**, *43*, 12118–12125. [CrossRef]
56. Zhong, Y.; Gu, Y.; Yu, L.; Cheng, G.; Yang, X.; Sun, M.; He, B. APTES-functionalized Fe_3O_4 microspheres supported Cu atom-clusters with superior catalytic activity towards 4-nitrophenol reduction. *Colloids Surf. A Physicochem. Eng. Asp.* **2018**, *547*, 28–36. [CrossRef]
57. Yang, T.; Zou, H.Y.; Huang, C.Z. Synergetic Catalytic Effect of Cu_2–x Se Nanoparticles and Reduced Graphene Oxide Coembedded in Electrospun Nanofibers for the Reduction of a Typical Refractory Organic Compound. *ACS Appl. Mater. Interfaces* **2015**, *7*, 15447–15457. [CrossRef]
58. Zou, X.; Fan, H.; Tian, Y.; Zhang, M.; Yan, X. Chemical bath deposition of Cu_2O quantum dots onto ZnO nanorod arrays for application in photovoltaic devices. *RSC Adv.* **2015**, *5*, 23401–23409. [CrossRef]
59. Demirci, S.; Sahiner, N. Superior reusability of metal catalysts prepared within poly(ethylene imine) microgels for H_2 production from $NaBH_4$ hydrolysis. *Fuel Process. Technol.* **2014**, *127*, 88–96. [CrossRef]
60. Balbay, A.; Saka, C. Effect of phosphoric acid addition on the hydrogen production from hydrolysis of $NaBH_4$ with Cu based catalyst. *Energy Sour.* **2018**, *40*, 794–804. [CrossRef]
61. Shi, D.; Zhu, G.; Zhang, X.; Zhang, X.; Li, X.; Fan, J. Ultra-small and recyclable zero-valent iron nanoclusters for rapid and highly efficient catalytic reduction of p-nitrophenol in water. *Nanoscale* **2019**, *11*, 1000–1010. [CrossRef]
62. Bae, S.; Gim, S.; Kim, H.; Hanna, K. Effect of $NaBH_4$ on properties of nanoscale zero-valent iron and its catalytic activity for reduction of p-nitrophenol. *Appl. Catal. B* **2016**, *182*, 541–549. [CrossRef]
63. Ali, F.; Khan, S.B.; Kamal, T.; Alamry, K.A.; Asiri, A.M. Chitosan-titanium oxide fibers supported zero-valent nanoparticles: Highly efficient and easily retrievable catalyst for the removal of organic pollutants. *Sci. Rep.* **2018**, *8*, 6260. [CrossRef] [PubMed]
64. Rajegaonkar, P.S.; Deshpande, B.A.; More, M.S.; Waghmare, S.S.; Sangawe, V.V.; Inamdar, A.; Shirsat, M.D.; Adhapure, N.N. Catalytic reduction of p-nitrophenol and methylene blue by microbiologically synthesized silver nanoparticles. *Mater. Sci. Eng. C* **2018**, *93*, 623–629. [CrossRef]
65. Sahiner, N.; Sagbas, S.; Aktas, N. Very fast catalytic reduction of 4-nitrophenol, methylene blue and eosin Y in natural waters using green chemistry: p(tannic acid)–Cu ionic liquid composites. *RSC Adv.* **2015**, *5*, 18183–18195. [CrossRef]
66. Lin, J.-Y.; Chen, P.-Y.; Kwon, E.; Oh, W.D.; You, S.; Huang, C.-W.; Ghanbari, F.; Wi-Afedzi, T.; Lin, K.-Y.A. One-step synthesized 3D-structured MOF foam for efficient and convenient catalytic reduction of nitrogen-containing aromatic compounds. *J. Water Process Eng.* **2021**, *40*, 101933. [CrossRef]
67. Shah, L.A.; Sayed, M.; Fayaz, M.; Bibi, I.; Nawaz, M.; Siddiq, M. Ag-loaded thermo-sensitive composite microgels for enhanced catalytic reduction of methylene blue. *Nanotechnol. Environ. Eng.* **2017**, *2*, 1–7. [CrossRef]
68. You, J.G.; Shanmugam, C.; Liu, Y.W.; Yu, C.J.; Tseng, W.L. Boosting catalytic activity of metal nanoparticles for 4-nitrophenol reduction: Modification of metal naoparticles with poly(diallyldimethylammonium chloride). *J Hazard Mater* **2017**, *324*, 420–427. [CrossRef]
69. Iqbal, K.; Iqbal, A.; Kirillov, A.M.; Wang, B.; Liu, W.; Tang, Y. A new Ce-doped MgAl-LDH@Au nanocatalyst for highly efficient reductive degradation of organic contaminants. *J. Mater. Chem. A* **2017**, *5*, 6716–6724. [CrossRef]
70. Li, Z.; Yuan, C.-G.; Guo, Q.; Wei, X. Preparation of stable AgNPs@PAN/GO-SH nanocompsite by electrospinning for effective degradation of 4-nitrophenol, methylene blue and Rhodamine B. *Mater. Lett.* **2020**, *265*, 127409. [CrossRef]
71. Qi, L.; Zhang, K.; Qin, W.; Hu, Y. Highly efficient flow-through catalytic reduction of methylene blue using silver nanoparticles functionalized cotton. *Chem. Eng. J.* **2020**, *388*, 124252. [CrossRef]
72. Hu, H.; Shao, M.; Zhang, W.; Lu, L.; Wang, H.; Wang, S. Synthesis of Layer-Deposited Silicon Nanowires, Modification with Pd Nanoparticles, and Their Excellent Catalytic Activity and Stability in the Reduction of Methylene Blue. *J. Phys. Chem. C* **2007**, *111*, 3467–6470. [CrossRef]
73. Khan, S.A.; Khan, N.; Irum, U.; Farooq, A.; Asiri, A.M.; Bakhsh, E.M.; Khan, S.B. Cellulose acetate-Ce/Zr@ Cu0 catalyst for the degradation of organic pollutant. *Int. J. Biol. Macromol.* **2020**, *153*, 806–816. [CrossRef] [PubMed]
74. Benali, F.; Boukoussa, B.; Ismail, I.; Hachemaoui, M.; Iqbal, J.; Taha, I.; Cherifi, Z.; Mokhtar, A. One pot preparation of CeO_2@ Alginate composite beads for the catalytic reduction of MB dye: Effect of cerium percentage. *Surf. Interfaces* **2021**, *26*, 101306. [CrossRef]
75. Gong, Z.; Ma, T.; Liang, F. Syntheses of magnetic blackberry-like Ni@ Cu@ Pd nanoparticles for efficient catalytic reduction of organic pollutants. *J. Alloys Compd.* **2021**, *873*, 159802. [CrossRef]
76. Vijayan, R.; Joseph, S.; Mathew, B. Green synthesis of silver nanoparticles using *Nervalia zeylanica* leaf extract and evaluation of their antioxidant, catalytic, and antimicrobial potentials. *Part. Sci. Technol.* **2019**, *37*, 809–819. [CrossRef]
77. Gul, S.; Khan, S.A.; Rehan, Z.A.; Akhtar, K.; Khan, M.A.; Khan, M.I.; Rashid, M.I.; Asiri, A.M.; Khan, S.B. Antibacterial CuO-PES-CA nancomposite membranes supported Cu0 nanoparticles for water permeability and reduction of organic pollutants. *J. Mater. Sci.* **2019**, *30*, 10835–10847. [CrossRef]
78. Sun, H.; Abdeta, A.B.; Zelekew, O.A.; Guo, Y.; Zhang, J.; Kuo, D.-H.; Lin, J.; Chen, X. Spherical porous SiO_2 supported CuVOS catalyst with an efficient catalytic reduction of pollutants under dark condition. *J. Mol. Liq.* **2020**, *313*, 113567. [CrossRef]

79. Sahu, K.; Singh, J.; Mohapatra, S. Catalytic reduction of 4-nitrophenol and photocatalytic degradation of organic pollutants in water by copper oxide nanosheets. *Opt. Mater.* **2019**, *93*, 58–69. [CrossRef]
80. Islam, M.T.; Saenz-Arana, R.; Wang, H.; Bernal, R.; Noveron, J.C. Green synthesis of gold, silver, platinum, and palladium nanoparticles reduced and stabilized by sodium rhodizonate and their catalytic reduction of 4-nitrophenol and methyl orange. *New J. Chem.* **2018**, *42*, 6472–6478. [CrossRef]
81. Sun, H.; Abdeta, A.B.; Kuo, D.-H.; Wu, Q.; Guo, Y.; Zelekew, O.A.; Yuan, Z.; Lin, J.; Chen, X. Activated carbon supported CuSnOS catalyst with an efficient catalytic reduction of pollutants under dark condition. *J. Mol. Liq.* **2021**, *334*, 116079. [CrossRef]
82. Wu, T.; Kou, Y.; Zheng, H.; Lu, J.; Kadasala, N.R.; Yang, S.; Guo, C.; Liu, Y.; Gao, M. A novel Au@ Cu_2O-Ag ternary nanocomposite with highly efficient catalytic performance: Towards rapid reduction of methyl orange under dark condition. *Nanomaterials* **2019**, *10*, 48. [CrossRef] [PubMed]